J. Mol. Biol. (1991) **219**, 335–358

Manganese Superoxide Dismutase from *Thermus thermophilus*

A Structural Model Refined at 1·8 Å Resolution

Martha L. Ludwig†, Anita L. Metzger, Katherine A. Pattridge and William C. Stallings‡

Department of Biological Chemistry and Biophysics Research Division University of Michigan, Ann Arbor, MI 48109, U.S.A.

(Received 26 October 1990; accepted 17 January 1991)

The structure of Mn(III) superoxide dismutase (Mn(III)SOD) from *Thermus thermophilus*, a tetramer of chains 203 residues in length, has been refined by restrained least-squares methods. The *R*-factor ($= \Sigma||F_o| - |F_c||/\Sigma|F_o|$) for the 54,056 unique reflections measured between 10·0 and 1·8 Å (96% of all possible reflections) is 0·176 for a model comprising the protein dimer and 180 bound solvents, the asymmetric unit of the $P4_12_12$ cell.

The monomer chain forms two domains as determined by distance plots: the N-terminal domain is dominated by two long antiparallel helices (residues 21 to 45 and 69 to 89) and the C-terminal domain (residues 100 to 203) is an $\alpha+\beta$ structure including a three-stranded sheet. Features that may be important for the folding and function of this MnSOD include: (1) a *cis*-proline in a turn preceding the first long helix; (2) a residue inserted at position 30 that distorts the helix near the first Mn ligand; and (3) the locations of glycine and proline residues in the domain connector (residues 92 to 99) and in the vicinity of the short cross connection (residues 150 to 159) that links two strands of the β-sheet. Domain–domain contacts include salt bridges between arginine residues and acidic side chains, an extensive hydrophobic interface, and at least ten hydrogen-bonded interactions.

The tetramer possesses 222 symmetry but is held together by only two types of interfaces. The dimer interface at the non-crystallographic dyad is extensive (1000 Å^2 buried surface/monomer) and incorporates 17 trapped or structural solvents. The dimer interface at the crystallographic dyad buries fewer residues (750 Å^2/monomer) and resembles a snap fastener in which a type I turn thrusts into a hydrophobic basket formed by a ring of helices in the opposing chain.

Each of the metal sites is fully occupied, with the Mn(III) five-co-ordinate in trigonal bipyramidal geometry. One of the axial ligands is solvent; the four protein ligands are His28, His83, Asp166 and His170. Surrounding the metal–ligand cluster is a shell of predominantly hydrophobic residues from both chains of the asymmetric unit (Phe86A, Trp87A, Trp132A, Trp168A, Tyr183A, Tyr172B, Tyr173B), and both chains collaborate in the formation of a solvent-lined channel that terminates at Tyr36 and His32 near the metal ion and is presumed to be the path by which substrate or other inner-sphere ligands reach the metal. A pocket adjoining the metal, formed by His33, Trp87, His83 and Tyr36, is postulated to be the substrate-binding site. Refinement of 2·3 Å data from crystals reduced with dithionite indicates that the co-ordination geometry at the metal is not changed by reduction.

Keywords: superoxide; superoxide dismutase; refinement; manganese(III); manganese(II); dimer; tetramer; domain interface

1. Introduction

The Mn and Fe-containing superoxide dismutases constitute a family of closely related proteins that are expressed in a wide variety of micro-organisms, including obligate anaerobes (Fridovich, 1979; Fee, 1980). The Mn enzymes are found universally in the mitochondria of eukaryotes; in human (see Harris *et al.*, 1980), *Saccharomyces cerevisiae* (Weisiger & Fridovich, 1973; Marres *et al.*, 1985) and presumably

† Author to whom all correspondence should be addressed.

‡ Present address: Monsanto Corporate Research, Mailzone BB4K, 700 Chesterfield Village, St Louis, MO 63198, U.S.A.

0022-2836/91/100335-24 $03.00/0

in other species, the structural genes are chromosomal. Complete amino acid sequences have been determined for at least 14 different species of Fe- or MnSODs† (Chan *et al.*, 1990; Thangaraj *et al.*, 1989), and X-ray structures reported for five of these enzymes: Fe-dismutases from *Pseudomonas ovalis* (Ringe *et al.*, 1983; Stoddard *et al.*, 1990) and *Escherichia coli* (Stallings *et al.*, 1983; Carlioz *et al.*, 1988), and Mn-dismutases for *Thermus thermophilus* (Stallings *et al.*, 1985), *Bacillus stearothermophilus* (Parker & Blake, 1988), and human liver mitochondria (Wagner *et al.*, 1989; and personal communication). The mitochondrial enzyme was obtained by expression from a recombinant construct in *E. coli* (Beck *et al.*, 1988).

In these superoxide dismutases catalysis proceeds by alternate one-electron reduction and oxidation of the trivalent and divalent metal species (Lavelle *et al.*, 1977; McAdam *et al.*, 1977) as shown (ignoring H^+):

$$\mathrm{Me(III)} + \mathrm{O_2^-} \rightarrow \mathrm{Me(II)} + \mathrm{O_2}$$
$$\mathrm{Me(II)} + \mathrm{O_2^-} \rightarrow \mathrm{Me(III)} + \mathrm{H_2O_2}.$$

It is usually presumed that catalysis involves formation of inner sphere complexes between O_2^- and the metal ion (Fee, 1980); ligation of the inhibitor, azide, to Fe(III) in crystals of FeSOD is consistent with this hypothesis (Stallings *et al.*, 1991). The Fe enzyme from *E. coli* has been the subject of a thorough kinetic analysis (Bull & Fee, 1985). The data support a mechanism in which oxygen is released after the first half-reaction between Fe(III)SOD and O_2^-, and peroxide is formed in a second half-reaction between Fe(II)SOD and O_2^-. Proton uptake accompanies the reduction of the Fe(III) enzyme, and proton transfer is partially rate-determining in the overall reaction. The turnover number (TN) for the consumption of two O_2^- per cycle is 26,000 s^{-1} at 25°C, and the TN/K_m (pH 8·4) value is 3×10^8 M^{-1} s^{-1}. The dependence of the rates on pH and on inhibitor concentration provides evidence for kinetically relevant pK values near 9·0 in both Fe(II) and Fe(III) species.

The behavior of MnSOD is more complex: the apparent TN value is much smaller (1300 s^{-1} at 25°C (Bull & Fee, 1985)) than for FeSOD, and two kinetic phases are observed when O_2^- generated by pulse radiolysis reacts with MnSOD (Pick *et al.*, 1974; McAdam *et al.*, 1977). These phenomena have suggested the formation of an unreactive species that becomes the dominant form of the enzyme during turnover at high substrate concentrations (McAdam *et al.*, 1977; Bull *et al.*, 1991). With the inclusion of a dead-end species, postulated to be a side-on complex of dioxygen, the kinetic data can be rationalized within the same mechanistic scheme proposed for FeSOD, without invoking the participation of oxidation states other than Mn(III) and Mn(II), suggested by Pick *et al.* (1974). The dependence of kinetic parameters on pH has not been fully investigated for MnSOD (Pick *et al.*, 1974; Bull *et al.*, 1991), and it is not known whether protonation is linked to reduction of the metal.

We reported the structure of MnSOD from *Thermus thermophilus* (Stallings *et al.*, 1985) at 2·4 Å resolution (1 Å = 0·1 nm); at that time the amino acid sequence had not been fully determined. Incorporating information from the protein sequence (Sato *et al.*, 1987) we have now refined the structure of the Mn(III) enzyme to a resolution of 1·8 Å with an R factor of 0·176 (for all data), and the structure of the Mn(II) enzyme to a resolution of 2·3 Å (R = 0·173). As a result, the co-ordination of the metal ions is more accurately determined, and the surroundings of the metal–ligand cluster, the interactions beteen monomers in this tetrameric molecule, and the putative entrance pathway for substrates can all be described in detail. Some of this information has been summarized in a recent symposium report (Stallings *et al.*, 1991). The Mn ions are embedded rather deeply in the protein, and accessibility probes show that the metal is shielded from solvent (or substrate) by a gateway formed by the conserved residues His32 and Tyr36. The distribution of charge in the vicinity of the Mn(III) strongly suggests that the fifth ligand, a solvent, may in fact be OH^- rather than H_2O. Comparison of the structures of the Mn(III) and Mn(II) oxidation states shows no evidence for reorganization of the metal–ligand cluster on reduction.

2. Experimental

(a) *Crystals and data collection*

Crystals were grown from ammonium sulfate at pH 7 as described (Stallings *et al.*, 1984), in space group $P4_12_12$ with $a = b = 146{\cdot}6$ Å and $c = 55{\cdot}6$ Å. The asymmetric unit houses 2 monomers, related by a local dyad, and designated as chains A and B. MnSOD tetramers form by association of A/B dimers across the crystallographic dyad.

The native data set used for refinement of Mn(III) dismutase to 1·8 Å was collected at the San Diego Area Detector Facility using 2 crystals (25°C), 1 at lower resolution, and another to extend data from 2·4 Å to 1·8 Å. Data from the first crystal include 91,578 observations of 24,547 unique reflections to 2·4 Å; the higher resolution data set comprises 214,205 observations of 48,957 reflections. The data sets were scaled and merged to yield 54,056 observations from 10·0 to 1·8 Å, representing 96% of the theoretical total.

$$R_{\mathrm{sym}} \; (= \Sigma_{hkl}\Sigma_i|I_i - \langle I\rangle|/\Sigma_{hkl}\langle I\rangle)$$

for the 2nd crystal was 0·066, and the merging R value was 0·075. Crystals of the *T. thermophilus* enzyme are remarkably stable to X-irradiation (Stallings *et al.*, 1984).

The Mn(II) data were also measured at San Diego using a crystal reduced with excess dithionite in holding solution buffered at pH 7. The oxidation state of the metal center could be assessed by visual observation, since the

† Abbreviations used: SOD, superoxide dismutase; A, B, C and D, designations for individual monomer chains where A,B and C,D are related by local symmetry, and A,C and B,D are related by crystallographic symmetry; r.m.s., root-mean-square.

Table 1
History of refinement

Run	Cycles	Resolution (Å)	Reflections	Atoms	Solvents†	*B*†	Occupancy‡	R_{start}	R_{end}
A	7	10–3·5	7556	3052	0	O	–	0·361	0·300
	3	6–3·0	10,665	3052	0	O	–	0·322	0·292
	4	5–2·4	20,067	3052	0	O	–	0·340	0·309
B	5	5–2·4	20,067	3052	0	I	–	0·304	0·276
C	6	5–1·8	52,284	3052	0	O	–	0·343	0·307
D	9	5–1·8	52,284	3052	0	I	–	0·291	0·269
E	3	5–1·8	52,284	3415	129	O	–	0·307	0·274
G	10	5–1·8	52,284	3415	129	I	+	0·266	0·192
H	5	15–1·8	55,406	3641	355	I	+	0·176	0·180
I	2	10–1·8	54,056	3639	353	I	+	0·179	0·178
J	6	10–1·8	54,056	3467	181	I	+‖	0·191	0·186
K	8	10–1·8	54,056	3468	182	I	+	0·190	0·187
L	6	10–1·8	54,056	3468	182	I	+‖	0·191	0·183
M	6	10–1·8	54,056	3468	182	I	+	0·184	0·185
N	8	10–1·8	54,056	3464§	178	I	+‖	0·186	0·176¶

† Solvents other than metal ligands; O, overall *B* refined; I, individual isotropic *B* refined.
‡ –, occupancies not varied; +, occupancies of solvents varied.
§ 124 atoms with occupancies set to 0·01.
‖ Occupancies and thermal factors of metal and its ligated solvent were refined.
¶ *R* between 2·0 and 1·9 Å, 0·217 (all data), 0·171 ($I > 2\sigma$); between 1·9 and 1·8 Å, 0·249 (all data), 0·175 ($I > 2\sigma$).

purple color characteristic of Mn(III)SOD is bleached on reduction (Fee *et al.*, 1976). The data set is 97% complete between 10·0 and 2·3 Å; $R_{sym} = 0·0404$ for 67,126 measurements of 24,379 reflections to 2·3 Å.

(b) *Starting model for refinement*

The structure of *T. thermophilus* MnSOD was initially determined by isomorphous replacement, and the first model was built into an averaged electron density map computed with multiple isomorphous replacement phases and data to a resolution of 2·4 Å (Stallings *et al.*, 1985). That model utilized a consensus of known sequences to fit the electron density, substituting alanine or glycine residues where side-chains were ambiguous. It was adjusted with the aid of interactive graphics, using the regularization (Hermans & McQueen, 1974) and real-space refinement options in FRODO (Jones, 1982), to produce a starting model for least-squares refinement. The *R* value for data between 5·0 and 2·4 Å was 0·340 (Table 1).

(c) *Refinement by restrained least-squares: general procedures*

The model was refined with the Hendrickson–Konnert PROLSQ programs (Hendrickson, 1985) using several different computers (Table 1). The initial calculations at low resolution (A and B in Table 1) were conducted on a VAX 730; cycles at higher resolution (runs C through L) were then calculated at the San Diego Supercomputer Center with a version of PROLSQ modified by Stuart Oatley to run on the Cray-XMP; the final cycles (runs M and N) were computed on a Silicon Graphics IRIS 4D/220 workstation. Reflection data were given unit weights throughout, and all measured data were retained, with no $\sigma(I)$ cutoff. Non-crystallographic symmetry restraints were not applied at any stage. Restraints on local geometry and non-bonded contacts were varied and weighted as described by Hendrickson (1985); the sigma values for bonded distances and standard deviations for the final cycles are given in Table 2. After steps D and G in Table 1, and between each of the runs following step I, adjustments to the model were made with interactive graphics using the programs FRODO (Jones, 1982) or TOM (Cambillau & Horjales, 1987) with appropriate difference maps (amplitudes $|3F_o|-|2F_c|$, $|2F_o|-|F_c|$ and $|F_o|-|F_c|$). The overall temperature factor was refined during lower resolution cycles (step A), after the extension to higher resolution (C) and after major rebuilding (E). At higher resolution, the isotropic atomic temperature factors were refined; for the solvents, occupancies and temperature factors were varied but only in alternate cycles. To prepare coefficients for omit maps, selected atoms were deleted by setting their occupancies to 0·01 for several cycles.

(d) *Progress of refinement*

The sequence of computations is summarized in Table 1. At step C (after a total of 19 cycles at lower resolution), the resolution was extended from 2·4 to 1·8 Å, adding approximately 32,000 reflections to the ~20,000 that had been refined. Our success in incorporating these

Table 2
Restraints and final r.m.s. deviations from ideality

Restraints	Number	r.m.s. Δ	Restraint σ
A. *Distances* (Å)			
Bond (1–2)	3390	0·019	0·015
Angle (1–3)	4612	0·042	0·025
Planar (1–4)	1274	0·060	0·035
B. *Non-bonded contacts*			
Single torsion	1347	0·192	0·500
Multiple torsion	955	0·199	0·500
Possible hydrogen bonds	234	0·161	0·500
C. *Torsion angles*†			
Planar (0°, 180°)	416	4·0	3·0
Staggered (±60°, 180°)	546	19·2	15·0
Ortho-normal (90°)	72	35·7	20·0

† 1034 of a possible 2006 were restrained. Last r.m.s. shift in position = 0·010 Å. Last r.m.s. shift in $B = 0·10$ Å^2.

data in a single step is attributed to careful construction of the starting model and to the quality of the data. After step D the protein sequence was reported (Sato *et al.*, 1987), and side-chains that had not been correctly identified were replaced. It was evident that a residue had been omitted at position 129 (glycine); correction of this omission required renumbering of the remainder of the sequence. The chain was also extended 2 residues beyond the C terminus that had been assigned in the 2·4 Å maps, in accord with the sequence information. We identified 129 solvents, and both solvent and protein atoms were further adjusted after another 13 cycles of refinement. The overall temperature factor was 19·9 Å^2 at the conclusion of step E. A major reduction in the R factor occurred at step G, where the full model was refined.

At step H, an additional 226 solvents were added to the model and the data from 15·0 to 5·0 Å were included in the calculations. The inner data were modified by the solvent correction factors (Bolin *et al.*, 1982), which are incorporated in the San Diego version of PROLSQ. The refinement behaved erratically until the data between 15·0 and 10·0 Å were removed. Further rounds (I through N) were carried out with data from 10·0 to 1·8 Å.

Before step J, the solvent atoms were re-examined. We chose a conservative approach to the inclusion of solvents. Any solvents that were isolated were rejected, i.e. each water molecule was required to belong to a network that could be traced back to the surface of the protein. Solvents whose scattering contributions were small were also rejected: the scattering contribution of each putative solvent at 2·0 Å resolution was required to be at least 30% of the scattering by an oxygen with full occupancy and $B = 18$ Å^2. This criterion for rejection thus takes into account both occupancy and B values (Kundrot & Richards, 1987). Finally, we did not include both sites when pairs of peaks were closer together than a short hydrogen bonding distance (2·4 Å). While a complete solvent model may be expected to include some sites that cannot be occupied simultaneously because of close proximity, we have effectively eliminated such secondary sites and have retained only the dominant ones. Crystals of MnSOD diffract to at least 1·5 Å, and more sophisticated modeling of the solvent should be feasible at this higher resolution.

For the final stages of refinement (K to N) the solvents were included according to the above criteria, and adjustments of side-chains were made. Of the 180 solvents in the asymmetric unit in model N, 66 pairs are related by local symmetry, occupying equivalent positions in the A and B chains. We selected orientations of Asn, Gln and His that seemed chemically reasonable and superimposed the A and B chains to inspect their correspondence. At step N, 8 cycles were computed omitting 124 atoms that resided in weak or ill-defined densities. The R factor decreased (Table 1) and the resulting omit maps located 7 of these 124 atoms, suggesting that continuation of this refinement strategy was unlikely to reveal many more atoms of the protein. The 117 side-chain atoms whose positions remain undefined in omit maps are located in the residues listed in Table 3. Inspection of Table 3 shows that the undefined side-chain atoms are mostly in lysine, glutamate and glutamine residues and are exposed to solvent.

For comparison with refinements that cite R factors with limits on intensities, we have also calculated R for the 29,150 reflections with $I > 2\,\sigma(I)$ for the range 10·0 to 1·8 Å; the value is 0·1647 for model N. The r.m.s. difference between main-chain and C^β atoms of the A and B chains after independent refinement provides one measure of the accuracy of the co-ordinates; this difference was 0·185 Å, an estimate close to that expected from Luzzati plots (Fermi, 1975) for other structures at 1·5 to 2·0 Å resolution (Karplus & Schulz, 1987; Lindqvist, 1989). Co-ordinates submitted to the Data Bank are taken from a refinement starting with the parameters of round M (Table 1) and including all atoms to maintain reasonable stereochemistry.

Table 3

Residues with some atoms undefined

Residue	Comments
Glu14	Multiple conformations, both chains
Arg88	Multiple conformations, both chains
Lys96	Multiple conformations, both chains
Ile162	Multiple conformations, both chains
Ile165	Multiple conformations, both chains
Lys175†	Multiple conformations, both chains
Ile187	Multiple conformations, both chains
Glu198†	Multiple conformations, both chains
Lys5	Ill-defined in both chains
Lys23	Ill-defined in A chain
Lys46	Ill-defined in both chains
Glu54	Ill-defined in both chains
Arg60	Ill-defined in both chains; in central cavity
Gln67	Ill-defined in both chains
Glu101	Ill-defined in B chain
Lys105	Ill-defined in both chains
Glu108	Ill-defined in both chains
Gln114	Ill-defined in both chains
Glu118	Ill-defined in both chains
Lys119	Ill-defined in A chain
Gln122	Ill-defined in both chains
Lys137	Ill-defined in A chain
Lys142	Ill-defined in A chain
Gln185	Ill-defined in both chains
Lys201	Ill-defined in A chain
Lys202	Ill-defined in both chains

† Participates in interdomain interactions.

(e) *Refinement of Mn parameters*

Ligand–metal bond lengths and angles at Mn were not restrained in the refinements. However, restraints between the Mn and non-bonded protein atoms, and between the solvent ligand and its neighbors, were invoked. Two different "van der Waals'" radii were used for Mn to test the effect of varying this parameter: the covalent radius of 0·72 Å (all refinements through step J) and a minimum radius of 0·01 Å, in step L (see Results and Discussion). The occupancy and thermal factors for Mn and its solvent ligand were refined in alternate cycles in steps J, L and N.

(f) *Refinement of Mn(II)SOD*

The structure of Mn(II)SOD was refined starting with the model of the oxidized enzyme obtained at step G of Table 1. To avoid bias in the electron densities corresponding to the solvent ligand and the 4 protein ligands, refinement was first conducted with the occupancies from the solvent, for the histidine rings, and for the Asp166 side-chain all set to 0·01. Maps with coefficients $(|F|_o - |F|_c)\exp(i\alpha_{omit})$ were then calculated to model the ligands. The resulting densities correspond closely to the ligand positions and geometries determined for the Mn(III) structure, suggesting that reduction results in very small, if any, changes in the geometry of the metal–ligand cluster. In subsequent cycles, ligands were

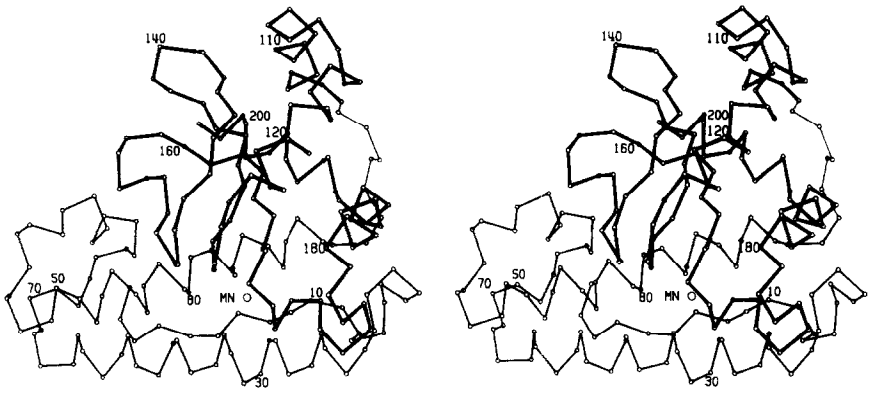

Figure 1. A drawing of the monomer of *T. thermophilus* MnSOD, with numbering corresponding to the protein sequence (Sato *et al.*, 1987). Residues 1 to 91 are assigned to the first domain and residues 100 to 203 (thick bonds) to the second domain. The thin bonds denote the intervening domain connector. The core of the A–B dimer interface is formed by residues of the second domain that are in the foreground of this view, i.e. sequences near 130, 150 and 169.

included in refinement, and the occupancy parameters of Mn(II) and of its attached solvent were varied, starting from values of 1·0 for Mn(II) and 0·5 for the solvent ligand. The metal remained at full occupancy, and the final occupancy for its solvent ligand approached 1·0 (see Results and Discussion).

(g) *Accessibility calculations*

The accessible surfaces of monomers, dimers and domains were determined according to the method of Lee & Richards (Richards, 1985) using the program ACCESS and a probe radius of 1·4 Å.

3. Results and Discussion

(a) *Monomer fold*

In this section we describe the substructures of the monomer fold, emphasizing features that are unusual or that may be related to stability or folding of Mn superoxide dismutase. For perspective, a stereo drawing of the monomer is presented in Figure 1. The division of the chain into two domains is based on distance plots, presented in earlier reports (Stallings *et al.*, 1985; Ludwig *et al.*, 1986) and recalculated here using the refined coordinates (Fig. 2(a)). The first domain (residues 1 to 91) is predominately α-helix, whereas the second domain (residues 100 to 203) is a mixed $\alpha+\beta$ structure. The two domains are linked by a single extending connector that lies on the surface of the molecule.

Figure 2(b) is a summary of the assignments of residues to various classes of secondary structure, as determined by the algorithm of Kabsch & Sander (1983), and Figure 2(c) is the Ramachandran plot of the ϕ,ψ angles for the backbones of both A and B chains. Scheme I compares the 14 known sequences of Mn- and FeSOD chains. Three-dimensional structures for the first three entries were used to align their sequences. The remaining alignments were performed with routines based on the algorithms of Lipman & Pearson (1985); the results are very similar to those given by Chan *et al.* (1990). The Mn-, FeSOD family of proteins is remarkably well preserved at the level of primary structure. Earlier investigations have demonstrated that the most variable regions occur at 45 to 70, near 140, and near 160 (*T. thermophilus* numbering: Carlioz *et al.*, 1988; Barra *et al.*, 1984).

(i) *The helices and the β-sheet*

Termini of the principal helices and sheet strands are indicated in Figure 2(b). The first long helix of domain I extends from Asp21 through Glu45, and is bent slightly by the insertion of a residue at position 30. In Figure 2(b) this irregularity appears as the assignment of a turn conformation at 31. This distortion, described earlier (Stallings *et al.*, 1985), allows two turns of helix to accommodate eight residues and aligns the side-chains of the metal ligand, His28, and the conserved Tyr36. The relative orientation of these residues may be important for efficient catalysis of superoxide dismutation, since it brings the hydroxyl group of Tyr36 close to the metal ion. Beyond residue 41 some of the $1\rightarrow4$ helical interactions are long and then the winding tightens to form a 3_{10} hydrogen bond between O44 and N47.

The C terminus of the first helix and the sequences immediately following are highly variable in dismutases from different species (Scheme I). In *T. thermophilus* this variable region extends from residue 42 through residue 72. From Pro48 to Leu65, the structure can be described as a ring of short helical repeats connected by turns or bends (Fig. 2(b)); this is the site for tetramer formation. The most regular part is a short α-helix (α_2), comprising residues 54 through 60. The second major α-helix of domain I (α_3) starts with residue 69, whose carbonyl oxygen is hydrogen-bonded to NH-73. Within this helix is a sequence (RNNGGG) that is not predicted to be helical by the standard algorithms (Brock & Walker, 1980).

The second domain begins with a pair of α-helices (residues 100 to 109 and 112 to 126) oriented approximately at right angles. The abrupt change in axial direction that separates these helices occurs at

```
                        10        20        30        40        50
Mn T. therm.  PYPFK LPDLG YPYEA LEPHI DAKTM EIHHQ KHHGA YVTNL NAALE KYPYL HGVEV
Mn Human       KHS LPDLP YDYGA LEPHI NAQIM QLHHS KHHAA YVNNL NVTEE KYQ-- EA-LA
Fe E. coli     SFE LPALP YAKDA LAPHI SAETI EYHYG KHHQT YVTNL N-NLI K---- -GTAF
Mn B. stear.   PFE LPALP YPYDA LEPHI DKETM NIHHT KHHNT YVTNL NAALE GHPDL QNKSL
Mn E. coli     SYT LPSLP YAYDA LEPHF DKQTM EIHHT KHHQT YVNNA NAALE SLPEF ANLPV
Mn H. halob.  SQHE LPSLP YDYDA LEPHI SEQVV TWHHD THHQS YVDGL NSA-E E-T-L -AENR
Mn M. leprae VAEYT LPDLD WDYAA LEPHI SGEIN EIHHT KHHAA YVKGV NDALA K---L DEARA
Mn S. cerev.   KVT LPDLK WDFGA LEPYI SGQIN ELHYT KHHQT YVNGF NTAVD QFQEL SDLLA
Mn Maize      VTTVT LPDLS YDFGA LEPAI SGEIM RLHHQ KHHAT YVANY NKALE Q---L E-TAV
Mn Mouse       KHS LPDLP YDYGA LEPHI NAQIM QLHHS KHHAA YVNNL NATEE K--YH EALAK
Mn Rat         KHS LPDLP YDYGA LEPHI NAQIM QLHHS KHHAT YVNNL NVTEE K--YH EALAK
Fe P. oval.    AFE LPPLP YAHDA LQPHI SKETL EYHHD KHHNT YVVNL N-NL- -VP-- GTPEF
Fe P. leiog.   AFE LPALP FAMNA LEPHI SQETL EYHYG KHHNT YVVKL N-GL- ----V EGTEL
Fe A. nidul.   SYE LPALP FDYTA LAPYI TKETL EFHHD KHHAA YVNNY NNAV- KDTDL DGQPI

                    60        70        80        90       100       110
Mn T. therm.  EVLLR HLAAL PQDIQ TAVRN NGGGH LNHSL FWRLL TP   GGA KEPVG ELKKA IDEQF
Mn Human       KGDVT AQI-- --ALQ PALKF NGGGH INHSI FWTNL SP   NGG GEPKG ELLEA IKRDF
Fe E. coli     EG--K SLEEI IRSSE GGVFN NAAQV WNHWF YWNCL AP   NAG GEPTG KVAEA IAASF
Mn B. stear.   EELLS NLEAL PESIR TAVRN NGGGH ANHSL FWTIL SP   NGG GEPTG ELADA INKKF
Mn E. coli     EELIT KLDQL PADKK TVLRN NAGGH ANHSL FWKGL KK   GTT LQ--G DLKAA IERDF
Mn H. halob.   ET-GD H-AST AGAL- GDVTH NGCGH YLHTM FWEHM SP   DGG GEPSG ALADR IAADF
Mn M. leprae   KD--D HSAIF LNEKN LAF-H LG-GH VNHSI WWKNL SP   NGG DKPTG GLATD IDETF
Mn S. cerev.   KEPSP ANARK MIAIQ QNIKF HGGGF TNHCL FWENL APESQGGG EPPTG ALAKA IDEQF
Mn Maize       SK--G DASAV VQ-LQ AAIKF NGGGH VNHSI FWKNL KPISEGGG EPPHG KLGWA IDEDF
Mn Mouse       GDVTT QV-AL ----Q PALKF NGGGH INHTI FWTNL SP   KGG GEPKG ELLEA IKRDF
Mn Rat         GDVTT QV-AL ----Q PALKF NGGGH INHSI FWTNL SP   KGG GEPKG ELLEA IKRDF
Fe P. oval.    EG--K TLEEI VKSSS GGIFN NAAQV WNHTF YWNCL SP   DGG GQPTG ALADA INAAF
Fe P. leiog.   AE--K SLEEI IKTST GGVFN NAAQV WNHTF YWNCL AP   NAG GEPTG EVAAA IEKAF
Fe A. nidul.   EAVIK AIAG- -DASK AGLFN NAAQA WNHSF YWNSI KP   NGG GAPTG ALADK IAADF

                        120       130       140       150
Mn T. therm.  GGFQA LKEKL TQAAM  GRFGS GWAWL VKD  PF  G K LHV LSTPN QDNP V
Mn Human      GSFDK FKEKL TAASV  GVQGS GWGWL GFN  KER G H LQI AACPN QDPL Q
Fe E. coli    GSFAD FKAQF TDAAI  KNFGS GWTWL VKN  SD  G K LAI VSTSN AGT PL
Mn B. stear.  GSFTA FKDEF SKAAA  GRFGS GWAWL VVN  N-  G E LEI TSTPN QDS PI
Mn E. coli    GSVDN FKAEF EKAAA  SRFGS GWAWL VLK  G-  D K LAV VSTAN QDS PL
Mn H. halob.  GSYEN WRAEF -EVAA  GA-AS GWALL VYD  PV  A KQLRN VAVDN HDE GA
Mn M. leprae  GSFDK FRAQF SAAAN  GLQGS GWAVL GYD  TL  GNK LLT FQLYD QQA NV
Mn S. cerev.  GSLDE L-IKL TNTKLA GVQGS GWAFI VKNLSNG  G K LDV VQTYN QD- TV
Mn Maize      GSFEA LVKKM NAEGA  ALQGS GWVWL ALD  KE  AKK VSV ETTAN QDP LV
Mn Mouse      GSFEK FKEKL TAMSV  GVQGS GWGWLG FNK  EQ  G R LQI AACSN QDPLQG
Mn Rat        GSFEK FKEKL TAVSV  GVQGS GWGWLG FNK  EQ  G R LQI AACSN HDPLQG
Fe P. oval.   GSFDK FKEEF TKTSV  GTFGS GWAWL VKA  D-  G S LAL CSTIG AGA PL
Fe P. leiog.  GSFAE FKAKF TDSAI  NNFGS SWTWL VKN  AN  G S LAI VNTSN AGC PI
Fe A. nidul.  GSFEN FVTEF KQAAA  TQFGS GWAWL VLD  N-  G T LKI TKTGN ADT PI

                            160       170       180       190       200
Mn T. therm.  M       E G  FT PIVGI DVWEH AYYLK YQNRR ADYLQ AIWNV L NWDV AEEFF KKA
Mn Human      G       TTG  LI PLLGI DVWEH AYYLQ YKNVR PDYLK AIWNV I NWEN VTERY MAC
Fe E. coli    T       T D  AT PLLTV DVWEH AYYID YRNAR PGYLE HFWAL V NWEF VAKNL LAA
Mn B. stear.  M       E G  KT PILGL DVWEH AYYLK YQNRR PEYIA AFWNV V NWDE VAKRY SEA
Mn E. coli    MGEAISGAS G  F- PILGL DVWEH AYYLK FQNRR PDYIK EFWNV V NWDE AAARF AAK
Mn H. halob.  L       W G  SH PILAL DVWEH SYYYD YGPDR GSFVD AFFEV I DWDP IAANY DDV
Mn M. leprae  S       L G  II PLLQV DMWEH AFYLQ YKNVK ADYVK AFWNV V NWAD VQSRY MAA
Mn S. cerev.  T       G P  LV PLVAI DAWEH AYYLQ YQNKK ADYFK AIWNV V NWKE ASRRF DAG
Mn Maize      T       K GASLV PLLGI DVWEH AYYLQ YKNVR PDYLN NIWKV M NWKY AGEVY ENV
Mn Mouse      T       T G  LI PLLGI DVWEH AYYLQ YKNVR PDYLK AIWNV I NWEN VTERY TAC
Mn Rat        T       T G  LI PLLGI DVWEH AYYLQ YKNVR PDYLK AIWNV I NWEN VSQRY IVC
Fe P. oval.   T       S G  DT PLLTC DVWEH AYYID YRNLR PKYVE AFWNL V NWAF VAEEG KTF
Fe P. leiog.  TE      E G  VT PLLTV DLWEH AYYID YRNLR PSYMD GFWAL V NWDF VSKNL AA
Fe A. nidul.  A       H G  QT PLLTI DVWEH AYYLD YQNRR PDYIS TFVEK LANWDF ASANY AAA
```

Scheme I. Structural and sequence alignments for 14 Mn and Fe dismutases. Positions are numbered to correspond to the sequence of *T. thermophilus* MnSOD and boldface is used to indicate residues that are identical to those in *T. thermophilus* MnSOD. For human MnSOD and *E. coli* FeSOD the insertions and deletions, relative to *T. thermophilus* MnSOD, have been assigned from the 3-dimensional structures. Even with the structural information, alignments are ambiguous in the region from residue 50 to residue 70. The remaining sequences have been aligned with *T. thermophilus* MnSOD using the algorithms of Lipman & Pearson (1985) and Pearson (1990), implemented in the program package

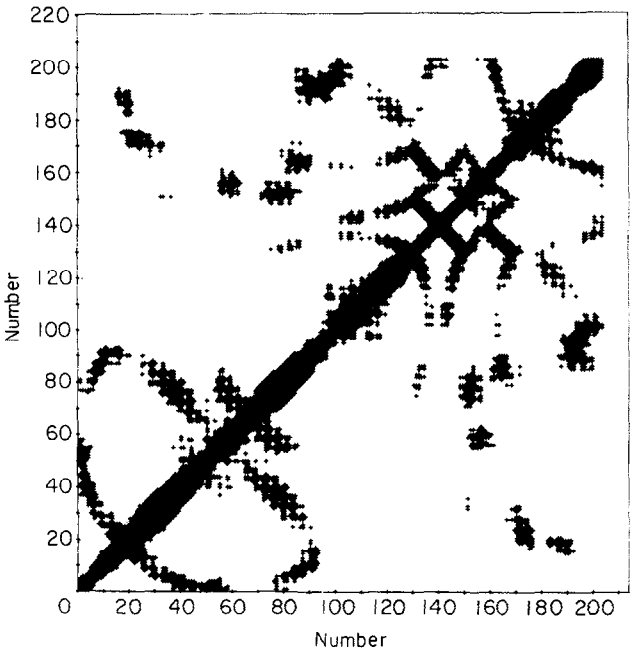

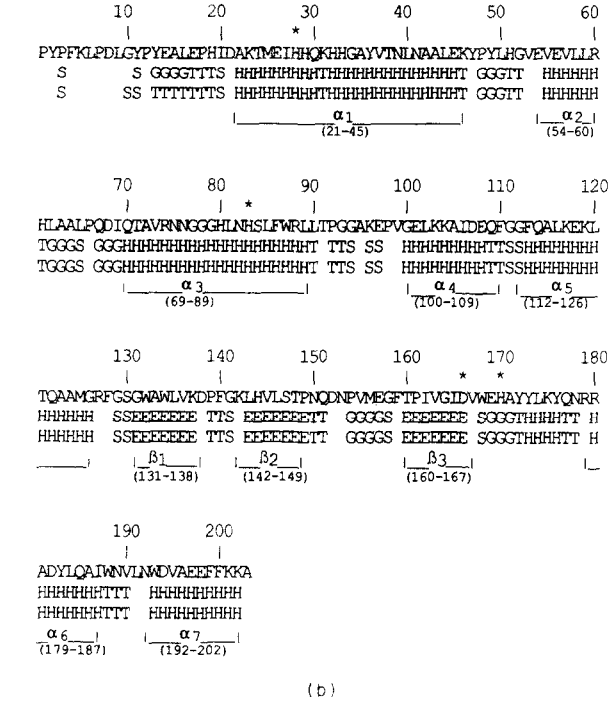

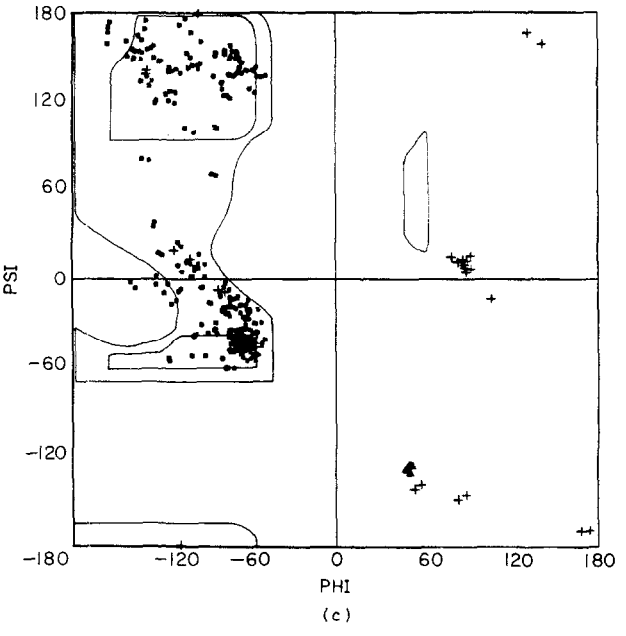

Figure 2. The conformation of the monomer chain. (a) A distance plot calculated from C^{α} co-ordinates, with a distance limit of 12 Å. The distribution of interactions provides the basis for the assignment of the domains shown in Fig. 1 and discussed in the text. (b) Analysis of residue conformations, using the DSSP program of Kabsch & Sander (1983). Conformations are coded according to the nomenclature of their paper: H, α-helix; E, sheet strand; G, 3_{10} helix; T, turn; S, bend. Conformations for residues from the A and B chains are given in lines 2 and 3, respectively; differences between the chains, which are related by local symmetry, occasionally lead to differences in assignments of residue conformations. Line 4 defines the boundaries of the major helices and sheet strands, as described in the text, and asterisks mark the metal ligands. Assignments made by the Kabsch–Sander algorithm often begin helices at the second residue whose carbonyl O participates in helical hydrogen bonding, and the criteria for hydrogen bonding are not stringent. Hence the ascriptions in line 4 differ somewhat from those of lines 2 and 3. In particular, the 3_{10} helices assigned at 13 to 16, 48 to 50, 62 to 64, 67 to 69 and 169 to 171 are better characterized as β-turns (see Table 4). (c) A Ramachandran diagram of the Φ,Ψ angles for the A and B chains. Glycine residues are indicated by the symbol +, and unexpected conformations by filled triangles. Thus, Asn150 and Gln177, at the second position of type II′ turns, are flagged with triangles in the lower right quadrant. Limiting contours for alanine are based on Ramachandran & Sasisekharan (1968).

MacVECTOR, with results similar to those given by Chan *et al.* (1990). Visual alignments were made near the C terminus, recognizing that this region is helical in the known structures: sequences extending beyond position 203 of *T. thermophilus* MnSOD are not shown. Assignments of helices and sheet strands are given in Fig. 2(b).

References for the sequence determinations are: Mn *T. thermophilus*, Sato *et al.* (1987); Mn human, Ho & Crappo (1988), Yaffa *et al.* (1987) and Heckl (1988); Fe *E. coli*, Carlioz *et al.* (1988) and Schinina *et al.* (1987); Mn *B. stearothermophilus*, Brock & Walker (1980); Mn *E. coli*, Steinman (1978), Takeda & Avila, (1986); Mn *Halobacterium halobium*, Tako *et al.* (1989); Mn *Mycobacterium leprae*, Thangaraj *et al.* (1989); Mn *Saccharomyces cerevisiae*, Ditlow *et al.* (1982) and Marres *et al.* (1985); Mn maize, White & Scandalios (1986); Mn mouse, Hallewel *et al.* (1986); Mn rat, Ho & Crapo (1987); Fe *Pseudomonas ovalis*, Isobe *et al.* (1987); Fe *Photobacterium leiognathi*, Barra *et al.* (1987); Fe *Anacystis nidulans*, Laudenbach *et al.* (1989).

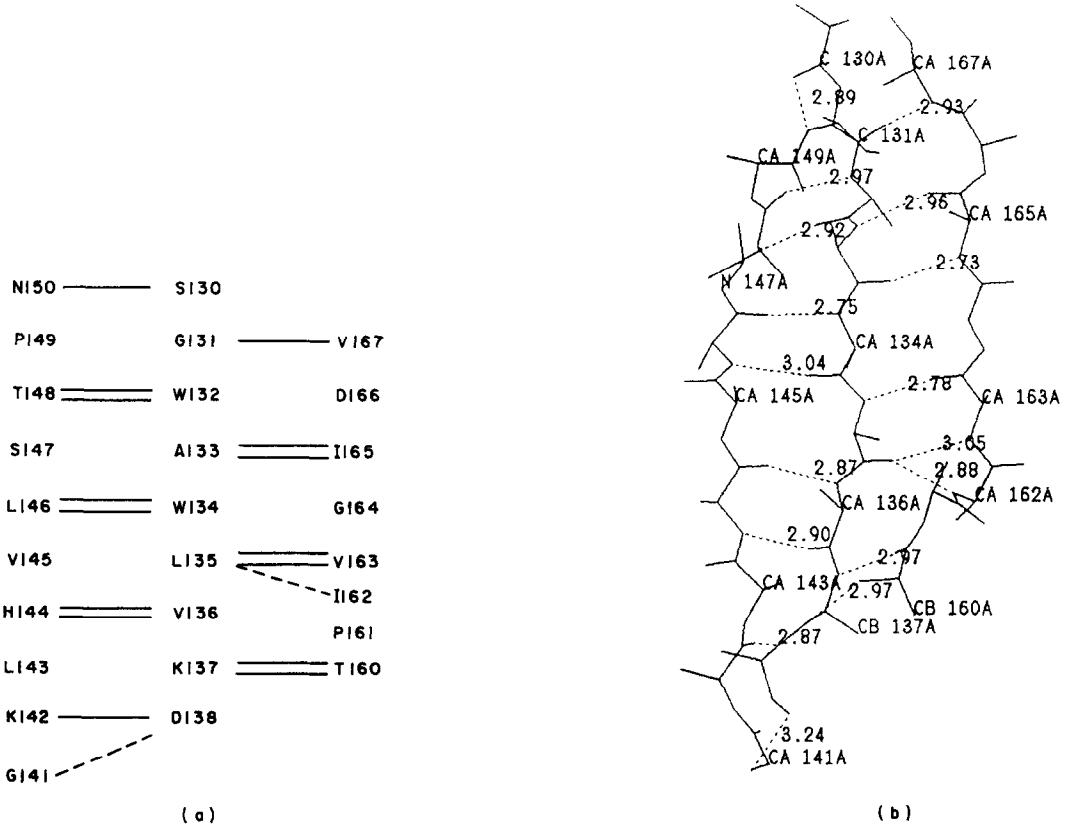

Figure 3. The antiparallel β-sheet region in MnSOD. (a) A schematic diagram indicating the positions of hydrogen bonds between the strands. (b) A drawing of the backbone and C^{β} atoms of the sheet, including the N → O distances. A bulge occurs at I162, with O135 hydrogen bonding to the amides of both 162 and 163. Following the type I turn at 139–140, Gly141 forms a bulge in the ladder of sheet hydrogen bonds. Residues 138 and 167 have been assigned as part of the sheet in Fig. 2(b). Asn150 is the second residue of a turn; its interaction with Ser130 maintains the pattern of hydrogen-bonding beyond the edge of the sheet. The turn at 139–140 protrudes into the A–C dimer interface, and Asp166, near the end of strand 3, is a metal ligand.

Gly111-Gly112 with Gly111 adopting a conformation typical of G1 bulges (see Table 5). Another pair of helices, at residues 179 to 187 and 192 to 202, ends the second domain. The first of these helical segments is terminated by 3_{10} hydrogen bonds at 186 to 189 and 187 to 190, and the intervening residue, Leu191, adopts a β conformation that produces a further change in direction between the two helices, whose interaxial angle is 73° (Richards & Kundrot, 1988). Although residues 173 to 176 are indicated as a single turn of α-helix in Figure 2(b), only two short 1→4 hydrogen bonds, at 172 to 176 and 173 to 177, are formed by this sequence, and we have not designated 172 to 176 as a separate α-helical unit.

The antiparallel sheet is diagrammed in Figure 3. The topology of this sheet is $+1, -2x$, recently termed "N-centered overhand" by Richardson & Richardson (1989). Other examples are found in rubredoxin (Watenpaugh *et al.*, 1980) and the ribosomal protein L7/L12 (Leijonmarck & Liljas, 1987). The diagram of Figure 3 includes all residues that contribute at least one interaction to the ladder of interstrand hydrogen bonds (Fig. 2(b), line 4). The sheet incorporates two bulges: the first occurs at Gly141 (see below), and the second is at Ile162, which has a conformation near the α region of the ϕ,ψ map (Richardson, 1981).

(ii) *Turns and bends*

Table 4A lists four β-turns that reverse the direction of the polypeptide chain; Table 4B lists addi-

Table 4
β-Turns and 1 → 3 interactions

Residues	Type	Φ_2,Ψ_2	Φ_3,Ψ_3	H-bond (Å)
A. *β-Turns in manganese superoxide dismutase*				
^{16}L-E-cP-H	VIa	−65, 150	−94, 11	2·93
^{138}D-P-F-G	I	−68, −11	−97, 9	3·24
^{149}P-N-Q-D	II′	50, −125	−106, 23	2·94
^{176}Y-Q-N-R	II′	49, −129	−77, −4	2·88
B. *Other hydrogen-bonded 1 → 3 interactions*				
^{12}P-Y-E-A	I	−57, −29	−90, 11	2·85
^{14}E-A-L-E	I	−66, −22	−102, 11	3·20
^{47}Y-D-Y-L	III	−55, −30	−66, −16	2·77
^{48}P-Y-L-H	I	−66, −16	−99, 3	2·87
^{50}L-H-G-V	I	−62, −17	−111, 22	3·33
^{61}H-L-A-A	III	−51, −42	−60, −22	2·93
^{62}L-A-A-L	I	−60, −22	−86, −16	3·12
^{66}P-Q-D-I	I	−55, −39	−73, −9	3·06
^{168}W-E-H-A	III	−59, −34	−59, −21	2·94

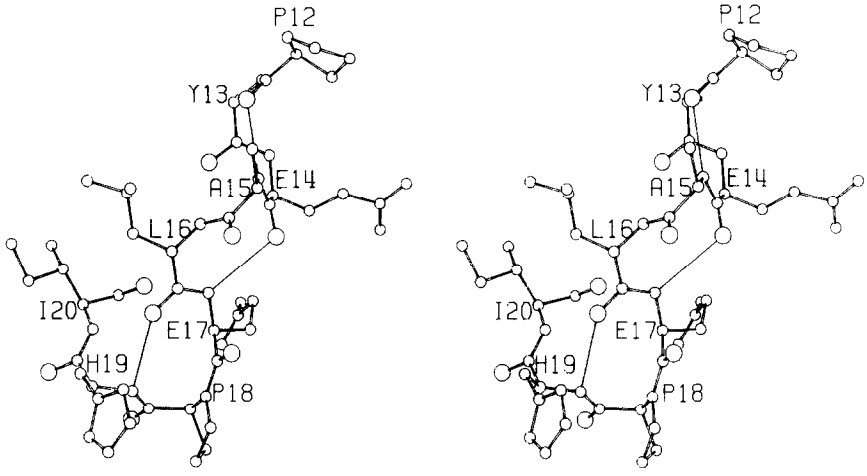

Figure 4. A stereo drawing of the region around the *cis* proline at position 18. Hydrogen bonds are presented as thin lines. The dihedral angles are those characteristic of a type VIa β-turn (Richardson, 1981) with hydrogen-bonding between O16 and N19. Residues 12 to 15 and 14 to 17 form 3_{10} turns preceding the *cis*-Pro turn (Table 4B). Hydrogen-bond distances and torsion angles for the A chain are listed in Table 4.

tional 3_{10} interactions (type I or type III), some of which occur in succession along the sequence. In the turn which begins at Glu17, an invariant proline (residue 18) adopts the *cis* conformation. The equivalent residue in FeSOD from *E. coli* is also *cis* (unpublished observations), and we surmise that the *cis* conformer occurs at this position in other SOD structures as well. The distance from O16 to N20 is 3·04 Å, so that the sequence ^{16}L-E-P-H-I may also be considered a three-residue turn (Milner-White & Poet, 1986). Figure 4 is a view of this region of the structure; between residues 15 and 21 the chain reverses direction sharply to accommodate packing of the N-terminal residues against the first long helix. The *cis* proline at position 18 would be expected to affect the kinetics of chain folding, and mutation of Pro18 might provide a test of the importance of packing at this turn to the stability of the fold.

The turn at 138 to 141 has a type I conformation, with a hydrogen bond between O138 and N141; however, Gly141 forms a bulge in the β-sheet (Table 5). This particular bulge turn arrangement is found in a number of hairpin or antiparallel sheet turns, as noted by Milner-White (1987), Sibanda & Thornton (1985) and Jones & Thirup (1986). Turns at 149 to 152 and 176 to 179 adopt the II′ conformation, despite the presence of Asn150 and Gln177 at the second position where glycine is normally preferred. Gln151 is involved in a network of interactions at the active site.

Table 5

Glycine conformations (A-chain)

Residue	Φ	Ψ	Comments
10	107	−14	
93†	91	17	Type II turn
100†	59	−140	Start of helix α_4
111†	95	5	Junction of helices α_4 and α_5
129†	90	−146	Bend preceding sheet (Fig. 5)
131†	174	−170	Start of sheet
141†	80	14	Bulge turn
158	92	10	Sheet cross connector (Fig. 6)

† Conserved.

The polypeptide chain also reverses direction at turns or bends that involve more than two residues. The most interesting of these bends is found between the end of helix α_5 at Gly126, and the beginning of the β-sheet at Gly131. This chain reversal is stabilized by a series of interactions between backbone oxygen atoms and the guanidinium group of Arg180 (Fig. 5).

(iii) *The sheet connector*

In the MnSOD from *T. thermophilus*, a cross connector (residues 150 to 159) packs against one side of the β-sheet and isolates residues of the sheet from contact with solvent. This is a relatively short connecting sequence, without meanders or α-helical excursions (Fig. 6). It includes the best example in MnSOD of 3_{10} helix. At residues 153 to 158 three successive hydrogen bonds can be formed, starting with O153–N156, and the dihedral angles for residues 154 to 156 are close to nominal values for a repeating 3_{10} structure. A hydrogen bond to Thr148 and contacts of Pro154 with Trp134 help to anchor the connector to the sheet. Comparison of known sequences shows some variability in the length and composition of this connector but a high frequency of proline and glycine residues. Pro161 is conserved and in the known structures is the second residue in sheet strand 3 (Fig. 3).

(iv) *Glycine and proline residues*

Half of the 16 glycine residues adopt conformations that map in the $+\phi$ region of Ramachandran plots; many of these appear to be conserved (Scheme I), suggesting that they play a role in determining the chain fold (Table 5). Three regions of the dismutase chain are relatively rich in proline

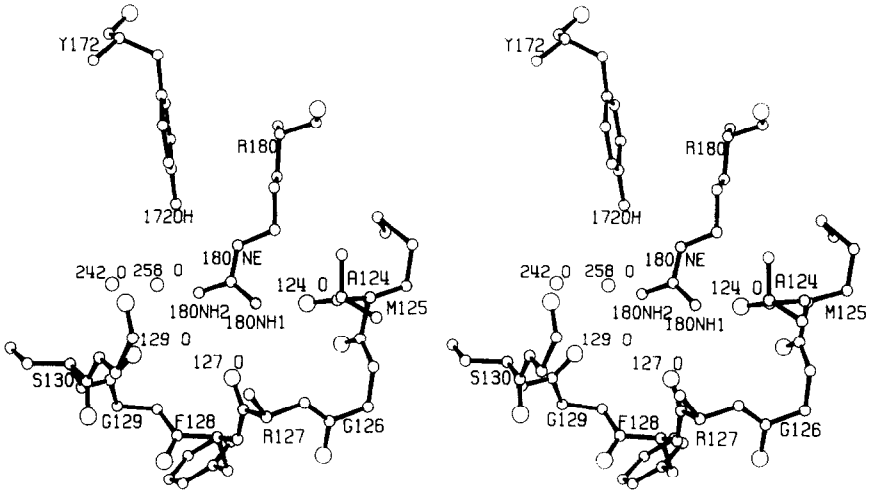

Figure 5. The interactions of Arg180 with the bend at residues 127 to 129. The sequence shown is ^{124}A-M-G-R-F-G-F-G, starting from the C terminus of helix α_5 and continuing to the beginning of sheet strand 1. The side-chain of Arg127 has been omitted from the drawing. The guanidinium group of Arg180 hydrogen bonds to Tyr172, to backbone carbonyls, and to solvents. Distances are: O172–NE180, 3·05 Å; O124–NH1180, 2·51 Å; O127–NH1180, 2·78 Å; O129–NH2180, 3·27 Å; O242–NH2180, 3·24 Å; and O258–NH2180, 3·18 Å. Glycine residues 129 and 131 have positive ϕ torsion angles (Table 5); Fig. 16 shows how these residues contribute to the substrate channel.

residues: the N terminus, the domain connector (see below) and the cross connector of the β-sheet. Five of the 13 proline residues of *T. thermophilus* MnSOD appear among the first 20 residues; other SODs are also proline-rich in this region. After the invariant Pro18, Pro7 (*T. thermophilus* numbering) appears most frequently. Among the mitochondrial SODs, which are processed for import, position 10 is often occupied by proline (Scheme I). In the *T. thermophilus* structure, Pro3, like Pro18, adopts the *cis* conformation.

(b) *The domain–domain interface and folding of the monomer chain*

The relative positions of the domain connector and the C terminus of the chain suggest that the domains probably fold separately, and come together late in the assembly of the molecule (Ludwig *et al.*, 1986) with the domain connector enclosing the C-terminal helices (Fig. 1). With the refined structure, we can examine in detail the domain interface and the interactions which posi-

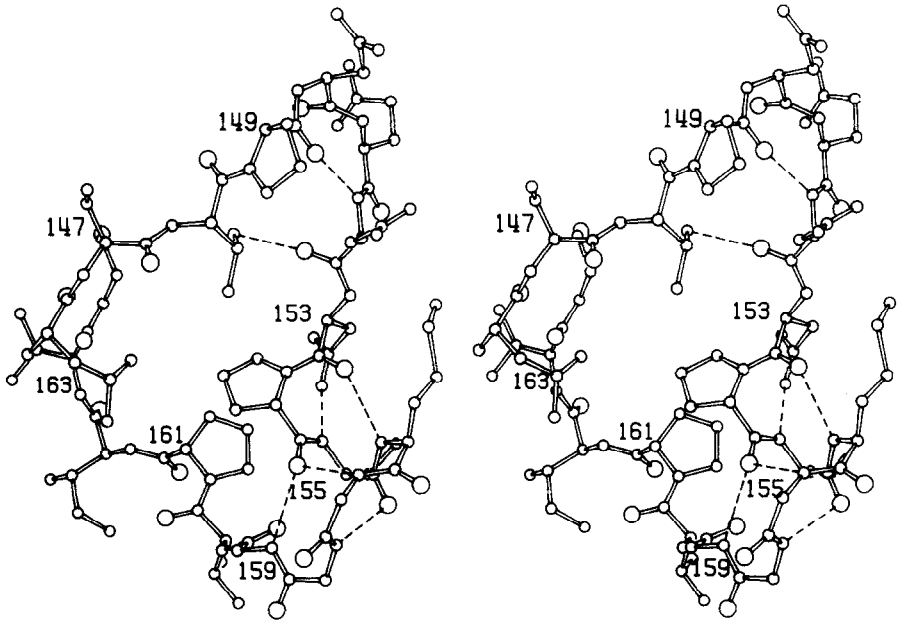

Figure 6. The cross connector between sheet strands 2 and 3. The sequence of residues on the right side is ^{149}P-N-Q-D-N-^{154}P-V-M-E-G-F-T-^{161}P. This rather short connector forms secondary structures, starting with a type II′ turn and including a short 3_{10} helix formed by residues 153 to 156. The helix interacts with the side-chain of Asn153 and a $1 \rightarrow 5$ hydrogen bond forms between 154 O and 159 N. Side-chain hydrogen bonds and non-polar contacts attach this sequence, which is partly exposed to solvent, to residues of the β-sheet. The side-chains of Val155, Glu157 and Phe159 have been truncated to clarify the view and the central strand of the sheet is not shown.

tion the C-terminal helices against domain I and the residues of the domain connector.

The contact surface between the two domains shows surprisingly little interpenetration of side-chains. Two arginine residues extend across the domain interface: Arg74 forms a well-defined salt bridge to Asp152, using NE and NH1; Arg88 is less firmly positioned near Glu198 (see Fig. 8). The total accessible surface that is buried when the domains are brought together, calculated as the difference in surface between individual domains and the monomer (omitting residues 93 to 99), is about 2500 Å^2. Extensive contacts between domains occur: (1) at the interface of the sheet and its cross-connector with portions of helix α_3; (2) at the interface of the *cis*-Pro turn and start of α_1 with the first C-terminal helix (α_6); and (3) at the Mn binding site (Figs 1 and 2(a)). At the center of the domain–domain contact is a hydrophobic core that includes residues Leu16, Ile20, Asn82, Leu85, Phe86, Leu89, Leu90, and Trp132, Trp134, Val163, Ile165, Tyr183, Ile187, Val190 and Leu191. The metal ion, with two protein ligands from each domain, serves as a bridge between domains, but the metal ligands are not involved in interdomain hydrogen bonds. Altogether, seven water molecules are trapped in the domain interface, with three of these acting as direct interdomain bridges. Included in this group is the solvent ligated to Mn, which makes multiple interactions with residues from domain II (see Fig. 12). Table 6 compiles the polar contacts made by these and other trapped water molecules, which constitute part of the interior of the protein structure. Among the ten interdomain hydrogen bonds (Table 7) is an interaction between the carbonyl oxygen of Leu89 and the peptide N of Asn192, which serves to position the pair of C-terminal helices with respect to the long helix, α_3,

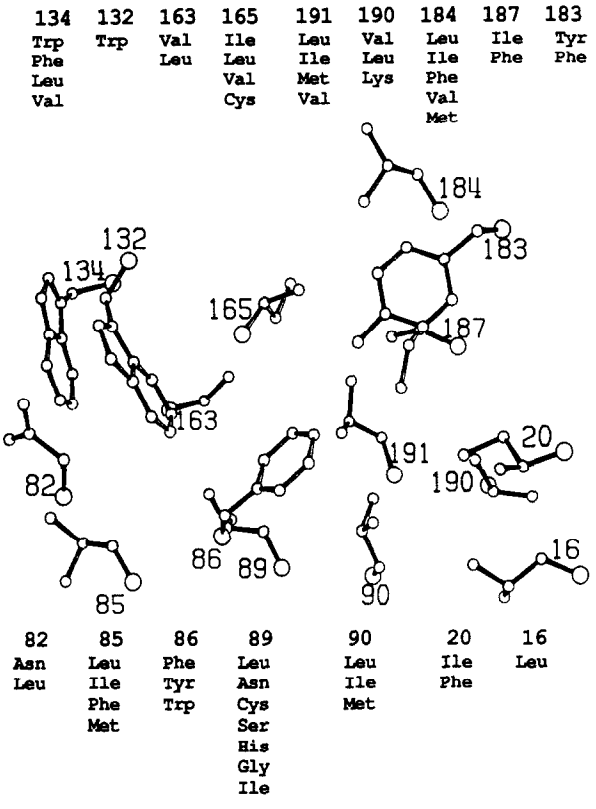

Figure 7. Residues constituting the interdomain core of MnSOD. The substitutions observed at each location are noted above (for domain II) and below (for domain I). None of these residues has significant exposure to solvent in the structure of *T. thermophilus* MnSOD. Lys at position 190 could project into solvent, but hydrophilic residues substituted for Leu89, near the center of the domain interface, must find suitable polar interactions.

Table 6
Structural solvents

Solvent	Polar neighbors	Location
205	Mn(III), Q151 NE2	Ligand to metal
210	A171 O, Y183 OH, 213 Wat	Domain interface
213	H28 ND1, 210 Wat	Domain interface
209	D21 OD1, T24 OG1, K175 N	Domain interface, bridge
233	T24 OG1, H170 O, L174 N	Domain interface, bridge
241	A171 O, 209 Wat	Domain interface, bridge
208	L16 N, I20 O, Y13 O	Intra-domain
215	W188 O, Wat193 NE1, K96 O	Intra-domain
219	Y2 N, L50 O, V53 O	Intra-domain
249	V99 O, Wat193 O, V99 N	Intra-domain
228	Y172 OH, E169 OE2	A–B interface
230	G129 N, 258 Wat	A–B interface
235	F128 O, S130 O, R127 NH1	A–B interface
239	N150 OD1	A–B interface
242	V167 O, G129 O, 258 Wat	A–B interface
258	R180 NH2, E169 OE2	A–B interface
269	Y173B OH, H170 O, H28 N	A–B and domain interfaces
270	169B OE1, 130 OG1, 169N	A–B interface
299	S130 N, N150 OD1	A–B interface, on dyad
225	Y49 OH, A64 O, D138C OD2	A–C interface
303	E157 O, A63C N	A–C interface
329	E157 O, H61C CD2	A–C interface

that terminates domain I. The orientation of these pieces of structure is further secured by hydrogen-bonding between O91 and the side-chain of Asn192, and by the juxtaposition of residues Val195, Glu198 and Phe199 with residues Arg88 and Leu89 (Fig. 8).

Comparison of the sequences in Scheme I shows that the salt bridges between domains are not conserved; Arg74 occurs in several thermophiles

Table 7
Domain–domain hydrogen bonds

Residue I	Atom	Residue II	Atom	Distance (Å)†
Pro18	O	Lys175‡	NZ	3·27
His19	O	Tyr176	OH	2·63
Tyr36	OH	Gln151	NE2	3·00
Arg74	NE	Asp152	OD2	2·80
Arg74	NH2	Asp152	OD1	2·74
Asn82	OD1	Asn153	ND2	2·68
Asn82	ND2	Gln151	O	3·08
Arg88†	NH1	Glu198	OE2	2·99
Leu89	O	Asn192	N	2·82
Thr91	O	Asn192	ND2	2·84

† Average of the A and B chains.
‡ These residues have multiple conformations: distances are closest contacts.

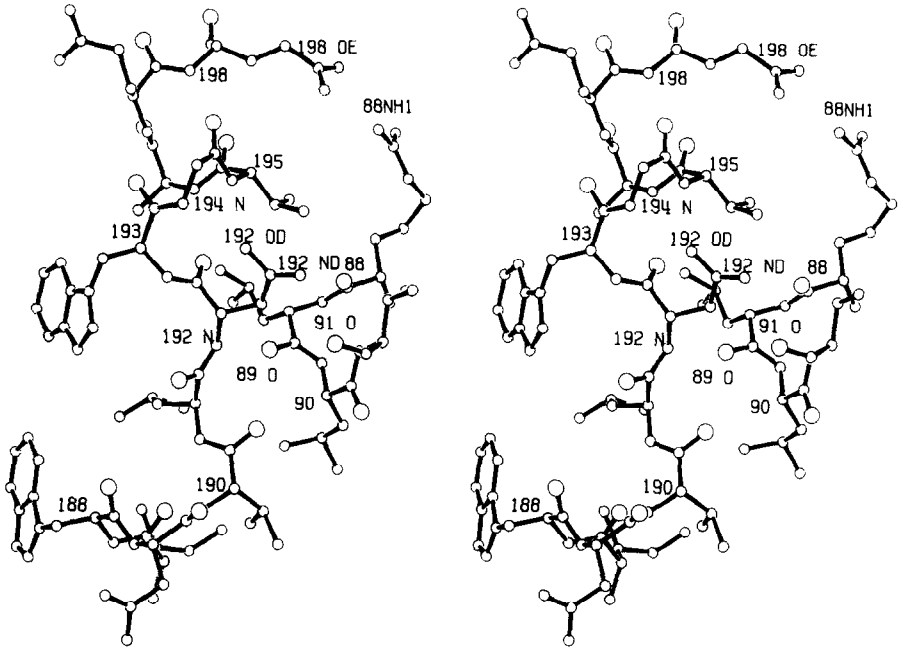

Figure 8. Interdomain contacts at the putative hinge region. A break in helical conformations occurs at the peptide 191–192, which is oriented to hydrogen bond to O89. The resulting elongation of the backbone occurs just where the domain connector wraps around the outside of residues 188 to 193, with Pro98 stacking against the indole ring of Trp193 (see Fig. 9). Hydrogen bonds connecting the domains are: O91–ND192, 2·80 Å; O89–N192, 2·82 Å.

(Scheme I) but the role of salt bridges in conferring thermostability has been challenged (Menendez-Arias & Argos, 1989). The patterns of conservation in the hydrophobic interdomain core of the molecule presumably reflect requirements for domain–domain interaction; Menendez-Arias & Argos (1989) have noted that in thermophiles domain interfaces seem to display increased hydrophobicity. Figure 7 includes the allowed interchanges of residues in the center of the domain interface, based on the sequences of Scheme I. The exchanges are reminiscent of those permitted in the folding cores of single domains (Bowie *et al.*, 1990). Whether these domain contacts influence the arrangement of the backbone in the individual domains is an interesting but open question.

Our hypothesis about folding of SOD implies that the domain connector, residues 92 to 99 in *T. thermophilus* MnSOD, acts as a hinge, and we presume that it has sufficient flexibility to allow the two domains to open and close and to "search" for a correct fit during folding. The domain connector sequences are dominated by glycine, proline and alanine residues. A precedent for flexibility in sequences rich in proline and alanine exists in the pyruvate dehydrogenase complex, where domains bearing the lipoyl groups are linked by mobile sequences whose lengths can vary from 7 to 32 residues (Texter *et al.*, 1988). According to the alignments of Scheme I, the domain connector in SODs varies in length from 7 (in *E. coli* MnSOD) to 11 residues. Curiously, the conformation of the connecting sequences is not conserved in the known dismutase structures. Parker & Blake (1988) have noted differences in the positions of the domain connector in MnSODs from *B. stearothermophilus* and *T. thermophilus*, and in Figure 9 we compare the domain connector in *T. thermophilus* MnSOD with the somewhat different connector found in FeSOD from *E. coli*. Domain connector–C-terminal interactions that may control positioning of the connector in the folded *T. thermophilus* protein included stacking of Trp193 with Pro98, hydrogen bonding of O95 to N193, and the bridge between the backbones of Thr91 and Asp194, formed by the conserved Asn192. However, comparisons with the structure of *E. coli* FeSOD show that the hydrogen bonds that position the connector vary from structure to structure.

(c) *The dimer interfaces*

(i) *The A chain–B chain interface*

The chains labeled A and B together constitute the asymmetric unit of the crystal. The non-crystallographic symmetry element relating them is a local dyad; superposition of the chains entails a rotation of 179·5° and a translation of 0·03 Å. The metal ions are 18·4 Å apart across this dyad, and the A/B pair of chains collaborates in forming the metal binding sites and substrate-entry channels for each of the active sites (see below). The dimer interactions involve residues from helix α_1, chain reversals at the end of the three strands of β-sheet, and residues located between the third strand of sheet and the start of helix α_6 (Fig. 1).

Viewed perpendicular to the dyad axis, the A–B interface presents layers of interactions (Fig. 10(a)). In the central region, two Ser130 residues are hydrogen-bonded to one another across the dyad, and farther from the axis OE1 of Glu169A makes a hydrogen bond to the nitrogen of Glu169B. Other

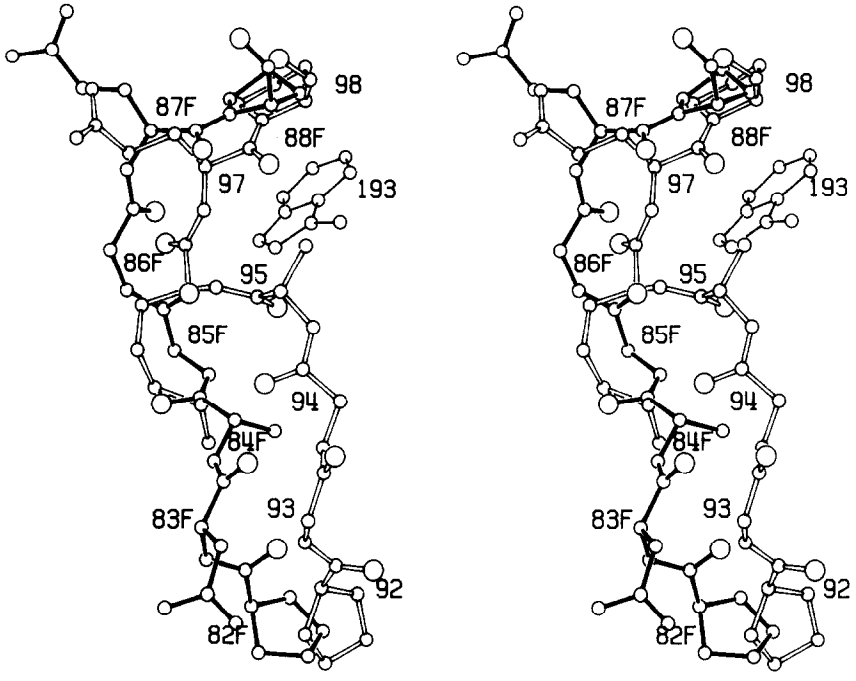

Figure 9. The conformation of the domain connector in MnSOD from *T. thermophilus*, compared with the corresponding region in FeSOD from *E. coli*. Atoms of FeSOD are connected by filled bonds, and C^{α} from FeSOD are labeled with a trailing F. In both structures, the proline at the C terminus of the connector stacks against an invariant tryptophan. In MnSOD, O95 hydrogen bonds to N193 but the equivalent interaction does not occur in FeSOD, where the connector instead forms an N85–O181 hydrogen bond. The structures were superimposed by a rigid-body transformation determined from least-squares minimization of differences between equivalent C^{α} atoms.

hydrogen bonds that link the two chains connect Glu169A with His170B, and His32A with Tyr173B. Each of these interactions is duplicated by the local symmetry, which is closely obeyed by all of the residues in the interface.

The interface incorporates 17 symmetry-related solvents which we term structural by the criteria that they are packed in the interface, contact at least two protein atoms and are not part of the outermost layer of clearly defined solvents (Table 6 and Fig. 10(a)). Most of these water molecules form bridges to the opposite chain *via* other solvents. Their occupancies are all greater than 0·70 and their temperature factors are less than 20 $Å^2$. Including these structural solvents in the list of atoms for computation of accessible surfaces we find that the total accessible surface that is buried upon formation of the A–B interface is about 2000 $Å^2$, or 1000 $Å^2$ per monomer. Approximately 12% of the accessible surface of each monomer is involved in the A–B interface.

Several residues penetrate across the interface and become part of the packing of the opposite chain: Asn178, Tyr173, Glu169 and Phe128 are the most striking examples (Fig. 10(a)). The interdigitation of the chains and the area of the interface imply that dissociation to monomers should be difficult. The formation of hybrid dimers of chains from *E. coli* Mn and Fe dismutases suggests that association–dissociation reactions do occur (Dougherty *et al.*, 1978; Clare *et al.*, 1984), but removal of metal from *B. stearothermophilus* MnSOD (Sato & Nakazawa, 1978) is insufficient to shift the equilibrium to the monomer form. Of the 17 residues comprising the interface (Fig. 10 and Table 8), eight are invariant and the remainder undergo conservative replacement, according to the 14 known sequences of Scheme I. Some of the pairwise substitutions that preserve the dimer interactions are discussed later in connection with the description of the substrate channel. The sequence homologies and the similarities of this dimer interface in the several known X-ray structures predict that dimer formation near the metals will be a constant feature of this class of SODs.

(ii) *The A chain–C chain interface*

Mn dismutases occur as tetramers in mitochondria and in a few micro-organisms such as *T. thermophilus* (Sato & Harris, 1977). We were puzzled at first by the observation that the sequences involved in tetramer formation in *T. thermophilus* MnSOD were in a variable region that did not align readily with sequences from the tetrameric human MnSOD. Recently, the structure of the human enzyme (U. G. Wagner, M. L. Ludwig, W. C. Stallings, M. M. Werber, C. Oefner, F. Frolow & J. Sussman, unpublished results) has revealed that its dimer–dimer packing is indeed very different from that found in MnSOD from *T. thermophilus*. Comparisons will be presented elsewhere.

Figure 11 depicts the tetramer and displays some details of the interfaces which form across the crystallographic 2-fold axis. The major interchain

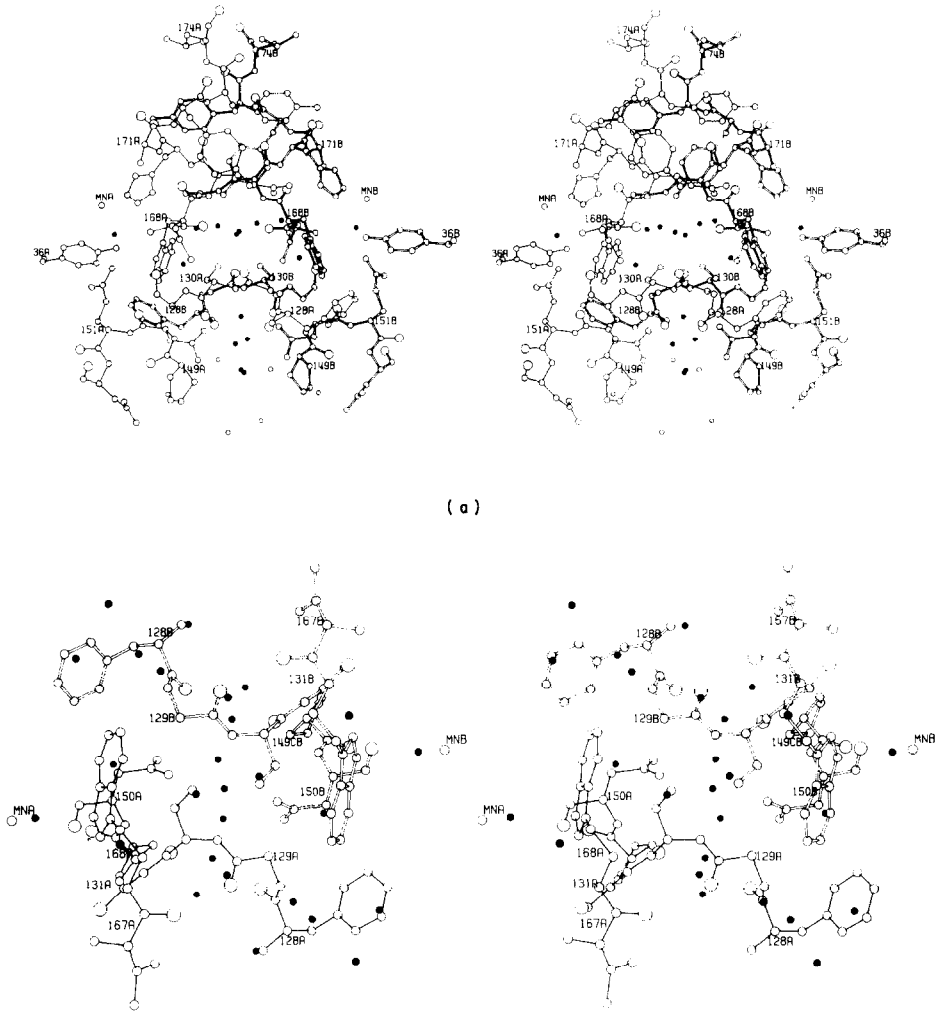

Figure 10. Stereo drawings of interactions around the local 2-fold axis relating subunits A and B. (a) A view perpendicular to the dyad, which is vertical in this drawing; the B chain atoms are connected by thick bonds. The A–B interface presents layers of interactions, beginning at the top with hydrophobic contacts between Leu174 and its symmetry mate. Just beneath are the Tyr173 side-chains and then residues Glu169 and His170. Below this level, approximately midway through the interface, one finds a layer of trapped water molecules separating the indole rings of residues Trp168, and the Ser130 residues hydrogen-bonded to one another across the dyad (see (b)). At the bottom, Asp150 interacts with its symmetry-related partner *via* water molecules, the upper one of which lies on the 2-fold axis. The water molecules designated as structural (Table 6) are filled in this drawing; other symmetry-related water molecules in or near the interface are represented as open circles. The side-chains of Phe128, Glu169, Tyr173 and Leu174 make multiple interchain contacts. Mn and Tyr36 are included for reference. (b) A view down the local dyad showing the region that is the lower part of (a) in more detail. The interaction between the hydroxyl groups of Ser130 can be seen at the center of the drawing; just below is a water molecule on the dyad, bridging the side-chains of Asn150. All of the solvent atoms associated with the "bottom" portion of the interface are filled in this view.

contacts are made between a basket of short helices, formed by residues 48 to 65, and the sequences 138 to 141 and 157 to 160 of the opposing chain (Table 8B and Fig. 11(b)). Three water molecules are incorporated in the interface (Fig. 11(c) and Table 6). The accessible area that is buried when the A–C contact forms is about 750 Å^2 per monomer. The tetramer of *T. thermophilus* MnSOD is a very open structure with an unusually large central cavity (Miller, 1989) and is held together by just two kinds of dimer interfaces, A–B and A–C. The only contact between the A and D chains is through solvents across the crystallographic dyad.

(d) *The metal-binding site*

(i) *The co-ordination geometry at Mn(III)*

The five Mn(III) ligands are arranged at the vertices of an approximate trigonal bipyramid (Table 9 and Figs 12, 13 and 14). Three of the protein ligands, NE2 of His83, OE1 of Asp166, and NE2 of His170, lie in the equatorial plane that is nearly perpendicular to the remaining two metal–ligand bonds. The metal ion is displaced only 0·03 Å from this trigonal plane. The largest departures from ideal geometry occur at the in-plane 170NE2–Mn–83NE2 and 83NE2–Mn–166O bond

Table 8
Major interchain contacts

Residue A	Residue B
A. *A chain–B chain neighbors*†	
Ile27	Tyr173
Ile27	Asn178
Lys31	Asn178
His32	Tyr173
Tyr36	Phe128
Asn75	Phe128
Phe128	Trp168
Phe128	Asn150
Phe128	Gln151
Gly129	Trp168
Gly129	Ser130
Ser130	Ser130
Trp168	Glu169
Glu169	Glu169
Glu169	His170
His170	Tyr173
Tyr173	Leu174
Gln177	Leu174
B. *A chain–C chain neighbors*‡	
Tyr49	Phe140
Val53	Phe140
His61	Pro139
His61	Phe140
His61	Gly158
Ala63	Glu157
Ala63	Phe159
Ala64	Phe159
Ala64	Asp138
Ala64	His144

† Contacts for 1 half-site; these are duplicated by local symmetry.
‡ Contacts for 1 half-site; these are duplicated by crystallographic symmetry

Table 9
Manganese co-ordination geometry

Bond length (Å)	Mn(III)†	Mn(II)†
Mn–28 NE2	2·11, 2·14	2·09, 2·18
Mn–83 NE2	2·12, 2·10	2·13, 2·10
Mn–166 OD1	1·75, 1·78	1·83, 1·84
Mn–170 NE2	2·16, 2·18	2·18, 2·23
Mn–205 O	2·07, 2·09	2·22, 2·24
Bond angle (deg.)	**Mn(III)†**	**Mn(II)†**
83NE2–Mn–166OD1	109·7, 109·9	109·2, 114·1
83NE2–Mn–170NE2	131·3, 133·8	130·0, 132·6
166OD1–Mn–170NE2	119·0, 116·2	120·5, 113·3
28NE2–Mn–2050	176·2, 172·2	172·2, 166·7
28NE2–Mn–83NE2	91·9, 94·0	93·0, 93·7
28NE2–Mn–166OD1	88·7, 86·3	90·1, 85·1
28NE2–Mn–170NE2	92·0, 90·6	92·1, 88·4

† First entry is for chain A, second for chain B.

angles, which are about 131° and 110°. These distortions might be dictated by the orientation of the metal ligands in the environment of the protein; similar angles are found in dichlorotris-(2-methylimidazole)Mn(II) (Phillips *et al.*, 1976). Bond distances and angles at Mn were not restrained during refinement (see Experimental); deviations in these lengths and angles, estimated from the agreement between the A and B chains, are ±0·013 Å and ±1·1°.

Despite the recent interest in the synthesis and properties of Mn(III) species (Wieghardt, 1989; Vincent & Christou, 1989), there are no model bipyramidal Mn(III) compounds with three imidazole and two oxygen ligands. The available database nevertheless provides some expectation values for Mn–ligand distances, which can be compared with our observations. In Mn(III)SOD, the average Mn–imidazole NE2 distance is $2{\cdot}13_5$ Å, and Mn–O distances are 1·76 and 2·08 Å (Table 9). Axial Mn–imidazole N distances are 2·18 Å in a square pyramidal complex of Mn(III) (Bashkin *et al.*, 1986) and 2·25 Å in dichlorotris-(2-methylimidazole)-Mn(II), a distorted trigonal bipyramid (Phillips *et al.*, 1976); the equatorial Mn–N bond lengths in the latter compound are 2·19 Å. In a square pyramidal Mn(III)–porphyrin–azide complex (Day *et al.*, 1975), the Mn(III) to N_{porph} lengths are 2·00 Å and the Mn–azide distance is 2·04 Å. Whereas the Mn–imidazole bond lengths in Mn(III)SOD are close to Mn–N distances found in model compounds, the Asp166 O^-–Mn bond is short. A survey of carboxylate–Mn distances shows that the shortest O–Mn bonds have lengths of 1·85 to 1·90 Å, if one excludes examples where the oxygen is a μ bridge. For instance, hexaco-ordinate malonate complexes of Mn(III) display bond lengths of 1·90 to 2·04 Å (Lis *et al.*, 1977). With data to 2·0 Å resolution, Stenkamp *et al.* (1983) estimated that differences among metal–ligand bond lengths in hemerythrin greater than 0·10 Å were probably significant. Using this criterion leads to the conclusion that the Asp166 O^-–Mn distance determined by refinement is distinctly shorter than the other four metal–ligand distances.

Refinement of atoms comprising metal binding sites poses some special problems. Although it is desirable to avoid imposing geometries on the metal–ligand cluster, refinement with no restraints may be underdetermined, especially for multinuclear clusters. In studies of hemerythrin, Stenkamp *et al.* (1983) included metal–ligand distance restraints but altered them to accord with shifts observed during refinement. For the Mn/Ca sites in concanavalin A, Hardman *et al.* (1982) employed unrestrained refinement followed by adjustment of protein geometry to nominal values. For MnSOD, we chose to restrain only the nonbonded distances involving Mn. It is difficult to determine the extent to which metal–ligand bond distances may be biased by this choice. Possibly, the oxygen of Asp166 can move toward the metal during refinement, whereas the histidine nitrogen atoms are more restrained by the van der Waals' contacts involving their adjoining carbon atoms and the solvent ligand is similarly restricted by its van der Waals' contacts with carbon atoms of His83 and

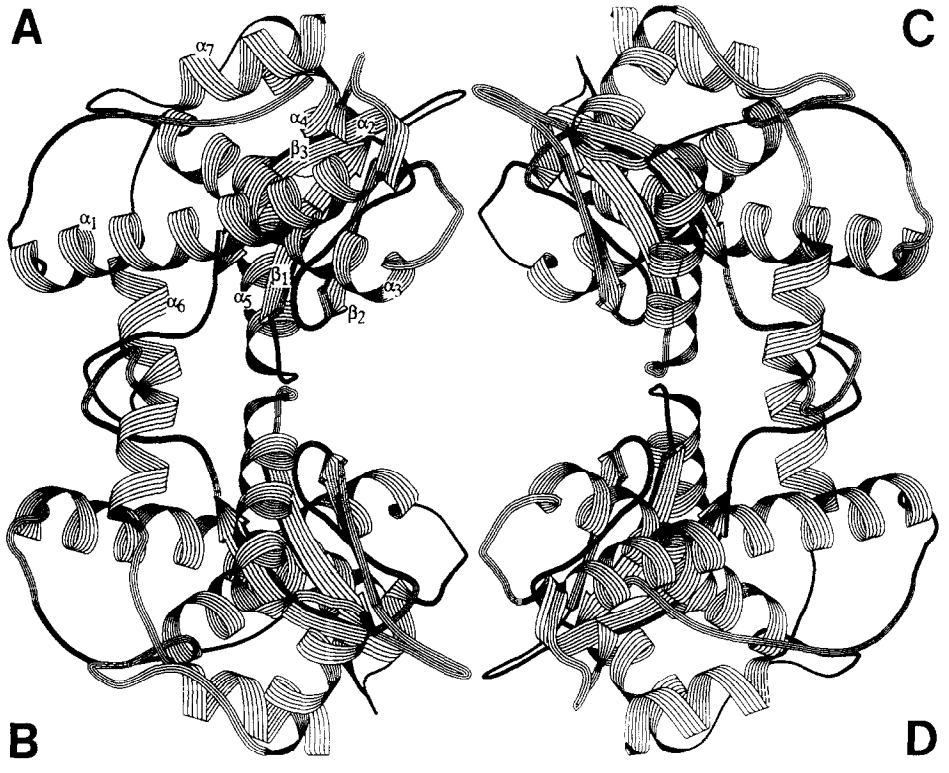
A
C
B
D
α7
α4
α2
β3
α1
β1
α3
α6
α5
β2

(a)

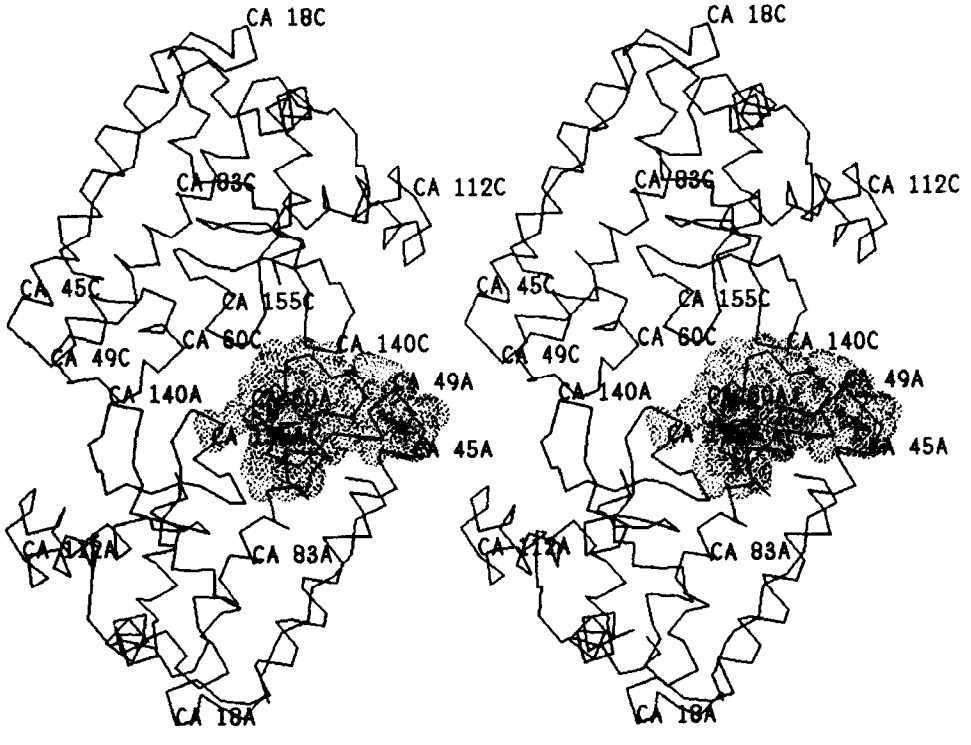
CA 18C
CA 83C
CA 112C
CA 45C
CA 155C
CA 60C
CA 140C
CA 49C
CA 140A
CA 49A
CA 45A
CA 83A
CA 18A
CA 18C
CA 83C
CA 112C
CA 45C
CA 155C
CA 60C
CA 140C
CA 49C
CA 140A
CA 49A
CA 45A
CA 83A
CA 18A

(b)

Fig. 11.

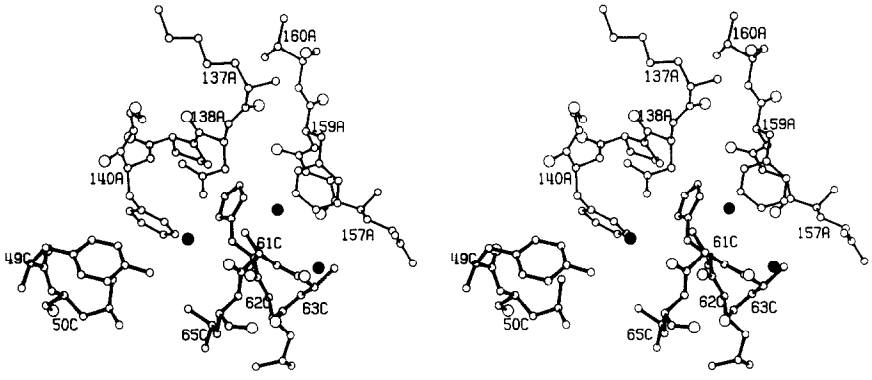

Figure 11. (a) A drawing of the arrangement of the chains in the tetramer of *T. thermophilus* MnSOD, prepared with the Protein Analysis Package (Callahan *et al.*, 1990). The crystallographic dyad is vertical, in the plane of the drawing, the local A–B dyad is horizontal. Chains are designated A to D as in the text; the equivalent A–C and B–D contacts around the crystallographic axis are shown in more detail in (b) and (c). This view emphasizes the large cavity in the center of the tetramer, and the absence of contacts between the A and D or B and C chains. (b) A view of the A–C chain interface, looking approximately along the crystallographic dyad. In this C^{α} representation one can see a circlet or basket of short helical regions (residues 49 to 65) into which is packed the turn at residues 139–140. One of the 2 symmetry-related helical baskets is surfaced, using all atoms, to illustrate the interchain packing. Residue 83, a metal ligand, indicates the separation of the Mn sites across the A–C dimer interface. (c) Details of the interactions around the crystallographic dyad. Backbone oxygen atoms are drawn with larger radii than the other atoms. Phe140A, in a β-turn, is surrounded by Tyr49, Leu50, His61, Ala64 and Leu65 from chain C. Three water molecules are an integral part of the interface: one hydrogen bonds to Tyr49C, Asp138A, and the carbonyl O to 61C; the 2nd bridges His61C and the O of 157A, and the 3rd packs between O157A and His61C.

His170. The refined bond distances are not very sensitive to the van der Waals' radius of Mn(III); changing the radius from 0·72 Å to 0·01 Å does not alter the metal–ligand distances by more than 0·025 Å.

(ii) *Occupancy of the metal site and evidence for solvent ligation*

Substoichiometric amounts of metal ions are often reported in analyses of Fe and Mn dismutases, and prior to the structure determinations, which demonstrated two distinct sites per dimer, there were proposals that the metal site might be shared between two monomers (Sato & Harris, 1977). It is not known whether metal is lost during isolation (perhaps from reduced enzyme) or not fully incorporated into the protein during folding. We investigated the metal content of crystals of *T. thermophilus* MnSOD by refinement of the occupancy parameters (steps J, L and N, Table 1). Occupancies and temperature factors were refined in alternate cycles for a total of 12 cycles. Occupancies remained near the starting values of 1·00, with final values of 1·00 for each of the two independent metal sites. The isotropic temperature factors converged to values of 10·2 and 9·9. Difference maps computed at the conclusion of step N (Table 1) were featureless at the metal ions at contour levels corresponding to 1 σ. Thus, the enzyme in crystals of *T. thermophilus* MnSOD appears to bind the full complement of Mn(III).

The solvent ligated to Mn(III) is about 3·3 Å from the Trp168 ring and is hydrogen-bonded to Gln151 (Table 10). We have suggested that the corresponding solvent ligated to Fe(III) in FeSOD is OH^-, and that this OH^- accepts a proton when the enzyme is reduced to the Fe(II) form (Stallings *et al.*, 1991). This mechanistic scheme, which assigns a functional role to the ligated solvent, may also describe the behavior of MnSOD. Hence the parameters for the solvent ligand were evaluated, both by refinement and by difference Fourier methods. Four cycles of refinement in which the scattering contribution of ligated solvent was omitted were used to verify the presence of the ligand in *T. thermophilus* Mn dismutase. ($|2F_o|-|F_c|$) maps computed after these cycles are displayed in Figure 13. In refinements including the scattering of ligated solvent, starting with occupancies of 0·5 at

Table 10

Hydrogen bonds and contacts in the metal-binding site

Residue	Atom	Residue	Atom	Distance†
His28	ND1	Wat213	O	2·69
His32	NE2	173B	OH	2·63
His33	ND1	Trp87	NE1	2·84
	NE2	His80	ND1	2·89
His83	ND1	Gly79	O	2·69
Gln151	NE2	Wat205	O	3·01
	NE2	Tyr36	OH	3·09
	OE1	Trp132	NE1	2·88
Asp166	OD2	Trp168	N	3·12
Trp168	NE1	Asn150	O	2·82
His170	ND1	Glu169B	OE2	2·82
Wat205	O	Trp168	CD1	3·28

† Average of A and B chains.

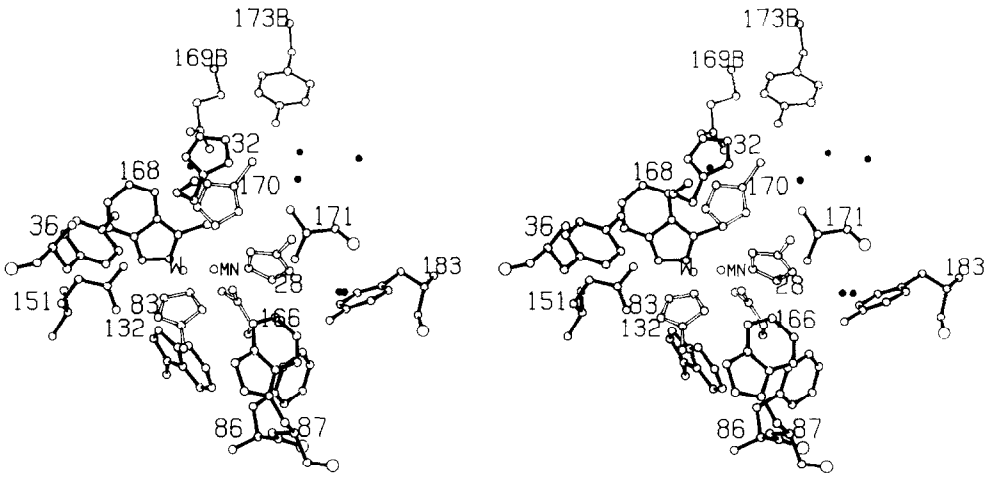

Figure 12. The metal ligands and the environment of the metal–ligand cluster, including structural water molecules adjoining the metal site (filled atoms). The metal ligands are drawn with open bonds. The equatorial plane of the trigonal bipyramid, containing Mn(III), the NE2 atoms of His83 and His170, and Asp166 OE1, is approximately vertical and tilted so that each of the ligand atoms is visible. The carboxyl group of Asp166 is stacked against the ring of Trp132, and the solvent ligand (W) contacts Trp168. Hydrogen bonds involving the ligands and adjoining residues are listed in Table 10, and contacts between aromatic rings are discussed in the text. The postulated path of approach of substrate is from above and left, passing by Tyr36 (see Fig. 16).

step J (Table 1), the solvent ligand increased in occupancy to an average of 0·99, while the isotropic thermal factors converged to 8·2 and 7·6 for the A and B sites, respectively.

In contrast, Parker & Blake (1988), in their study of partly refined MnSOD from *B. stearothermophilus* at 2·4 Å resolution, found no evidence for a solvent ligand, although the geometry of the protein ligands was essentially the same as for *T. thermophilus* MnSOD. Their refinement used sulfur-scattering factors to model partially occupied Mn(III) sites, and it is conceivable that a partly occupied solvent site was somehow obscured. Solvent is ligated to iron in refined structures of *E. coli* iron superoxide dismutase (Stallings *et al.*, 1991).

(iii) *Interactions and properties of the metal–ligand cluster*

Figure 12 shows the Mn(III)–ligand cluster and its surroundings. The ligands participate in several hydrogen bonds which may be important for stability and catalytic activity (Table 10). The ND1 atoms of His83 and His170 are donors to the carbonyl O of 79 (not shown) and to the carboxylate oxygen of 169B, respectively. These interactions suggest that neither His83 nor His170 can be

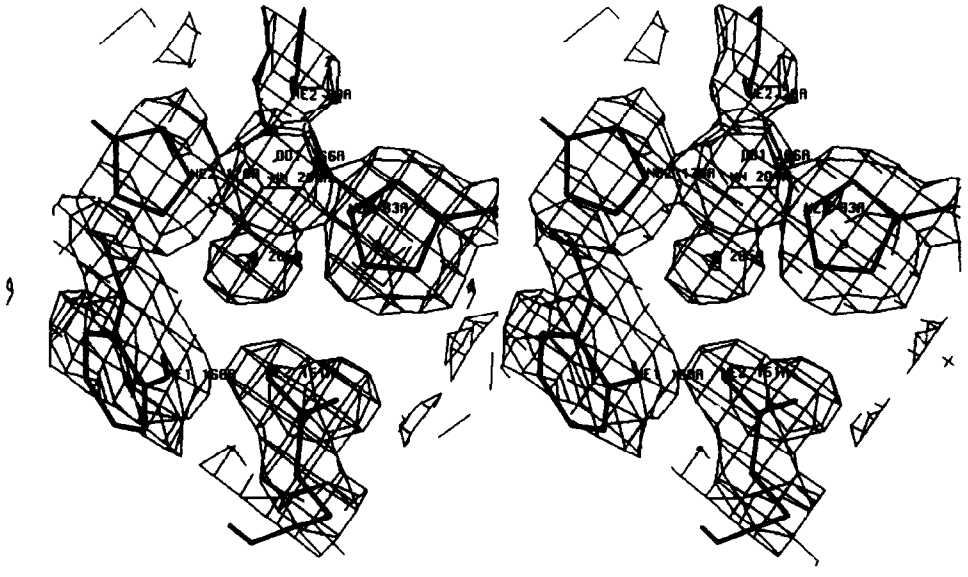

Figure 13. Electron density of Mn(III)SOD in a map calculated with coefficients $(|2F_o|-|F_c|)\exp(i\alpha_{omit})$ after refinements from which solvent 205 was deleted. Corresponding maps with amplitudes $(|F_o|-|F_c|)$ display a positive peak at the position of 205 O at a contour level of 10 σ. The clarity of the electron density at the conclusion of refinement is evident from this illustration.

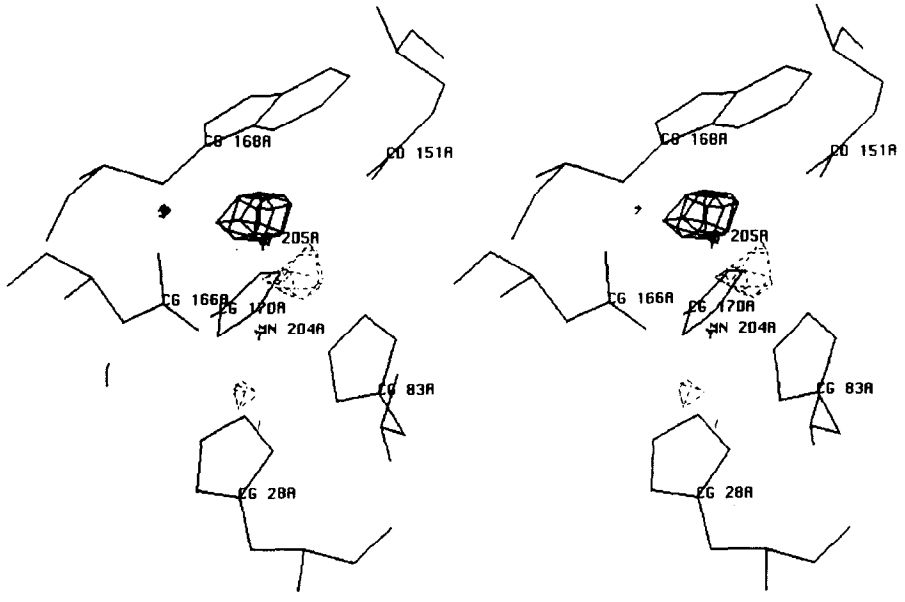

Figure 14. A difference map computed with amplitudes ($|F_{Mn(II)}| - |F_{Mn(III)}|$) and phases from the refined Mn(III)SOD structure and contoured at $\pm 1\ \sigma$. The absence of features at the protein ligands indicates that the metal co-ordination is unchanged on reduction. Positive (continuous lines) and negative (broken lines) peaks near the solvent ligand are consistent with a small displacement toward Asp166 OD2, detected by refinement. These features are less obvious in difference maps of the B-chain.

present as the anionic (imidazolate) species at pH 7. Two trapped water molecules (Fig. 12) adjoin His28: we cannot unequivocally assign the ionization state of this histidine from its surroundings, but suggest that His28 is also a neutral imidazole. We assume Asp166 is ionized; OD2 of Asp166 is 3·5 Å from Mn(III); it interacts with the backbone NH of Trp168 and with the solvent ligand. If our assignments of the ionization states of the protein ligands are correct, the formal charge of the Mn(III) metal center, embedded in a relatively hydrophobic environment, would be +2 if the solvent ligand were H_2O. The nearest compensating countercharge is found at Glu169B, about 7 Å away. We therefore consider it likely that the solvent ligand in the Mn(III) dismutase and in the homologous Fe(III) enzyme is OH^- rather than H_2O, so that the formal charge on the metal (III)–ligand cluster is +1 at neutral pH.

A series of aromatic residues from both chains dominates the environment of the metal–ligand cluster (Fig. 12). The indole NH of the tryptophan residues is a hydrogen bond donor: Trp132 to OE151, Trp168 to Asn150O, and Trp87 to His33ND1. Tyr173B and Tyr36 interact with His32 and Gln151, respectively (Table 10). Tyr36 and His32 together prevent access of solvent (and by analogy, substrate) to the metal or its ligands (see below). Networks of interactions made by these latter two residues may be important for catalysis: Tyr36 is connected *via* Gln151 to the solvent bound at Mn, providing a route by which the ionization of Tyr36 may interact with the charge on the metal–ligand cluster. In several ring–ring contacts, aromatic groups are approximately perpendicular to one another (Burley & Petsko, 1988). These packing contacts are made by Trp87, which is lodged between His28 and His29, and by Trp132, between His83 and Phe86. Phe86 in turn touches Tyr183 with the two ring planes oriented at right angles.

Conservation of residues at the metal site is remarkable, with comparisons based on 14 sequences from Mn and Fe enzymes (Scheme I). The four metal ligands are invariant, as are histidine residues 32 and 33, tyrosine residues 36 and 173, tryptophan residues 87, 132 and 168, and Glu169. Phe86 may be replaced by Tyr or Trp and Tyr183 may be replaced by Phe. Gln151 has a structural counterpart in FeSODs at 79 (*T. thermophilus* numbering), noted earlier (Carlioz *et al.*, 1988). MnSOD from *H. halobium* has a histidine residue at position 151; this side-chain can be placed into the structure so that the histidine nitrogen atoms correspond to the Gln OE1 and NE2 atoms, but the CE1 then makes close contacts with other atoms in the metal-binding site, suggesting that this mutation may perturb somewhat the packing at the metal center.

(iv) *The metal center in Mn(II) superoxide dismutase*

The structure of dithionite-reduced enzyme was determined in order to look for changes in co-ordination geometry or other reorganization that might accompany reduction. Reduced enzyme is an intermediate in the generally accepted mechanism for superoxide dismutation, and proton uptake is linked to reduction of the metal in FeSOD (Bull & Fee, 1985). The metal ligands are possible sites for this linked protonation, which requires pK values to differ in the oxidized and reduced forms of the enzyme. Binding of a proton by a neutral imidazole ligand (see above) would be expected to result in

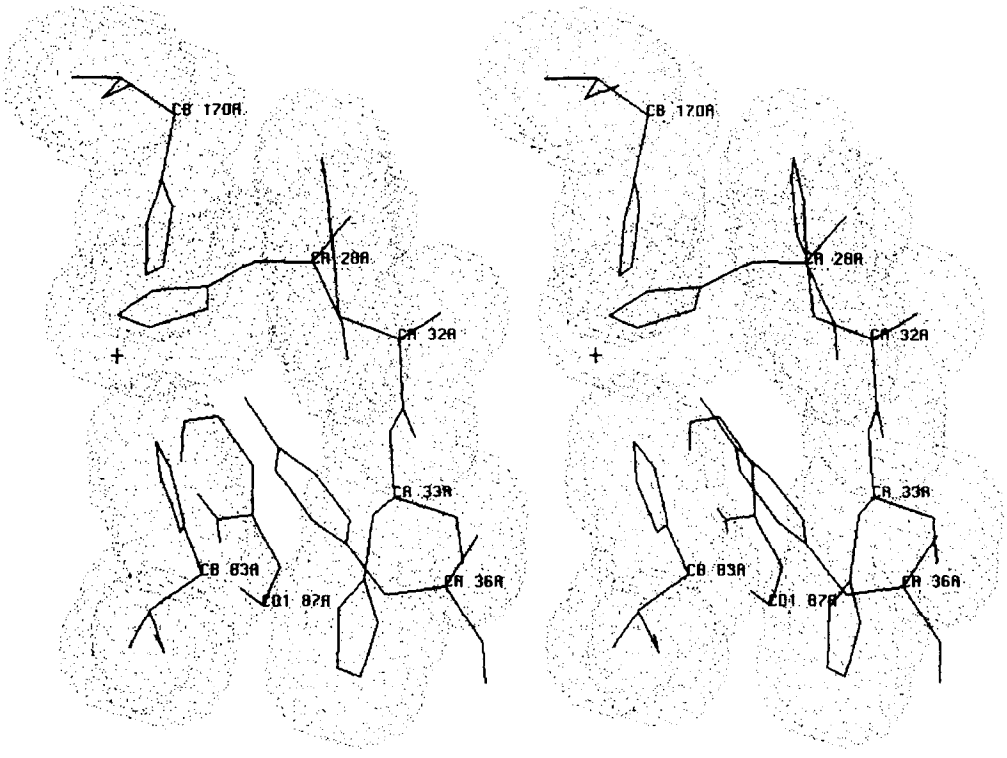

Figure 15. The presumed substrate binding site, a cavity formed by imperfect packing of main and side-chain atoms of His83, His33, Tyr36, His28 and Trp87. The position of Mn(III) is marked (+); the solvent ligand is not shown. In FeSOD, azide binds in the corresponding pocket, increasing the co-ordination number to 6 (Stallings *et al.*, 1991). This view shows how Tyr36 may act as a cap to the pocket.

displacement from the metal ion (Bertini *et al.*, 1985), and should therefore be evident as a structural perturbation in the Me(II) species.

To obtain an unbiased image of the metal ligands in reduced SOD we refined the Mn(III) model against data from the reduced crystal, omitting atoms of the ligands (see Experimental). None of the five ligands is displaced from Mn(II); densities in $(|F_o|-|F_c|)$ maps correspond to positions of the ligands in Mn(III) dismutase. This finding precludes a mechanism in which neutral imidazole ligands serve as proton acceptors. Difference Fourier maps with coefficients $(F_{red}|-|F_{ox}|)\exp i\alpha_{ox}$, shown in Figure 14, lead to the same conclusion, and suggest a shift of the ligated solvent toward Asp166, indicated by refinement to be about 0·15 Å. This shift would be consistent with the protonation of OH^- on reduction, as proposed in a mechanism for FeSOD (Stallings *et al.*, 1991), although such a protonation has not been directly demonstrated in MnSOD. After refinement of the Mn(II)SOD structure with data between 10·0 and 2·3 Å, the bond lengths and analyses differ slightly from those for oxidized enzyme (Table 9). Although the differences are within the error in bond lengths, the trend is toward increased bond lengths as expected on reduction of the metal.

(e) *Substrate binding and catalysis*

(i) *The substrate-binding site*

In experiments with Fe(III)SOD, utilizing azide as a substrate analog (Fee *et al.*, 1981), we found azide co-ordinated to the metal with its distal nitrogen atoms occupying a site between two histidine residues. The azide complex of Fe(III)SOD is six-co-ordinate with distorted octahedral geometry; the His73 ligated to Fe moves slightly to accommodate an azide nitrogen atom in the equatorial plane, but the axial solvent ligand is not displaced (Stallings *et al.*, 1991). In the uncomplexed structure, the site occupied by azide is a cavity created by imperfect packing, surrounded by His26, His31 and His73, Tyr34 and Trp77 in FeSOD. The equivalent region in MnSOD is shown in Figure 15. From studies of the azide complex of FeSOD we suggest that the cavity is a preformed "pocket" for substrate. It seems to be empty in the free enzymes; in maps of Mn(III)SOD at difference density levels of 1 σ there are no features in the center of the pocket. Some residual positive density is observed at a site adjoining the metal, but too close to represent bound solvent. The similarity of the Mn- and FeSOD structures leads us to propose that during turnover O_2^- binds to the metal in end-on fashion in both enzymes, expanding the co-ordination number to six.

However, the modes of inhibition appear to be different for Mn and Fe dismutases. Unlike FeSOD, MnSOD forms a dead-end complex during turnover (Bull *et al.*, 1991). The properties of this complex suggest a side-on interaction of dioxygen with the metal, rather than the end-on complexation inferred for catalytic intermediates. Azide is a weaker inhibitor of MnSOD than of FeSOD by an order of magni-

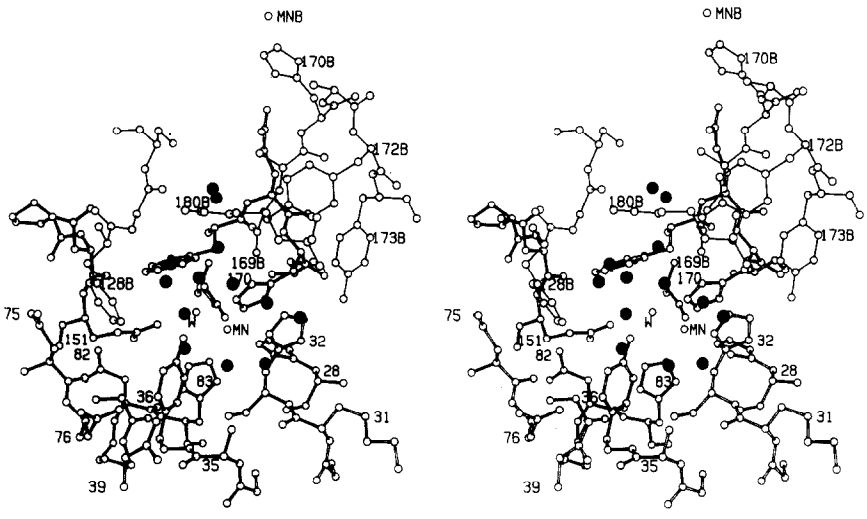

Figure 16. The substrate-entry channel, viewed approximately along its axis. Atoms of residues from the A chain are connected with thicker bonds; B chain residues (thinner bonds) form the upper and right boundaries of the channel. The positions of bound solvent molecules are indicated as filled circles. Met125 has been omitted from the drawing, and MnB included for reference (reproduced from Stallings *et al.*, 1991). The projection of the local dyad, relating the 2 Mn atoms, is approximately horizontal in this view.

tude. Difference Fourier maps of an azide complex of Mn(III)SOD at 4·0 Å reveal a positive peak bounded by residues His32, Tyr36 and His170, and the solvent ligated to Mn. The density partly overlaps the azide site modeled in FeSOD, but seems too far from the metal to permit co-ordination of azide. However, changes in optical and MCD spectra, observed on addition of azide to Mn(III)SOD from *E. coli* (J. W. Whittaker, private communication), suggest ligation to the metal ion. Interactions of inhibitors with MnSOD deserve further investigation.

(ii) *The substrate channel*

Examination of the structure suggests a route by which O_2^- can reach the metal ion. A funnel, or channel, that is open to solvent extends from the surface of the molecule to residues Tyr36, His32 and Glu169B, which adjoin the metal–ligand cluster. The channel is depicted in Figure 16 and a cross-section through the outer layers showing van der Waals' surfaces is displayed in Figure 17. The walls of the channel are formed by residues from both chains of the fundamental dimeric unit found in all Fe and Mn dismutases, although the axis of the channel is approximately perpendicular to the local dyad. Solvents lining the channel (Fig. 16) interact with both main and side-chain atoms. In *T. thermophilus* MnSOD the channel entry comprises Arg180 and Met125 of the B chain, and Asn39, Asn75 and Asn76 of the A chain. Moving inward toward MnA, a substrate or ligand might approach Phe128B, Tyr172B, Asn178B or Lys31A, and would finally encounter His32A or Tyr36A.

Calculations and displays of accessible surfaces (Richards, 1985) indicate that residues 32 and 36 prevent access of water to the metal ion, and imply that displacements of His32 and/or Tyr36 are required for superoxide or other ligands to form inner sphere complexes with the metal ion. Simulations of the reaction of superoxide with Fe or Mn dismutases (Sines *et al.*, 1990) confirm the inaccessibility of the metal site in the static structures; removing Tyr36 allows substrate to reach Mn.

Residues lining the channel may serve two roles: stabilization of the dimer interface and/or facilitation of substrate binding. It is thus not surprising that many are invariant or semi-invariant (Scheme I). Basic residues at the outer positions, Arg180B and Lys31A in *T. thermophilus* MnSOD, presumably increase the rate at which substrate binds (Sines *et al.*, 1990). His32, deeper in the channel, and hydrogen-bonded to Tyr173B, may also furnish a positive charge that guides anionic

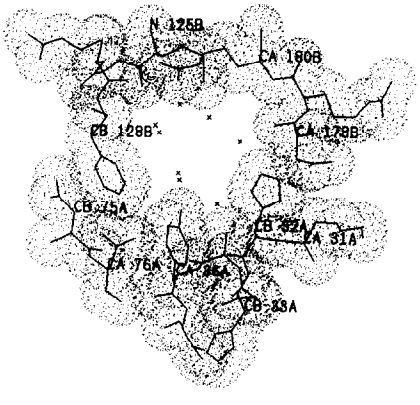

Figure 17. A section through the outer opening of the substrate channel, showing how the A and B chains interact to form the entrance to the channel. Residues 128B and 178B stack against 75A and 31A, respectively. Water molecules (labeled x), line the channel. Sequences shown are ^{31}K-H-H-G-A-Y-V from helix α_1, ^{75}N-N from helix α_3, ^{125}M-G-R-F from the loop preceding the β-sheet, and ^{178}N-R-R from the turn preceding helix α_6.

species to the metal. Chemical modification of arginine (Borders *et al.*, 1989; Chan *et al.*, 1990) or lysine (Benkovic *et al.*, 1983) residues is known to impair the catalytic activity of manganese or iron enzymes from *E. coli*. Arg180B, which contacts only B-chain residues, may be replaced by lysine, as in yeast MnSOD, but Lys31 and His32 are more highly conserved, perhaps because they contribute to the A–B chain interactions as well as to formation of the substrate channel. A semiconservative pairing occurs between Phe128B, which protrudes into the substrate channel of the A chain and Asn75A. These side-chains stack against each other to make part of the A–B chain interface. In yeast and human MnSODs, Gln replaces Phe128B and Phe substitutes for Asn75A to preserve the interchain stacking interaction.

The structure of the metal–ligand cluster and features of the substrate channel have several implications for the mechanism of catalysis or superoxide dismutation. Electrostatic effects mediated by residues in the substrate channel probably facilitate entry of substrate, as suggested for Cu/Zn dismutase (Bacquet *et al.*, 1988). But in addition, the net charge on the metal–ligand center, embedded in a relatively hydrophobic environment, may play an important role in mediating proton uptake and donation during the reaction cycle (Stallings *et al.*, 1991). The metal appears less accessible in Mn or Fe dismutases than in the Cu/Zn enzyme, and residues at the end of the substrate channel gate the approach of ligands; possibly this feature accounts for the reduction in V_m/K_m in the iron and manganese enzymes, relative to Cu/Zn dismutase (Bull & Fee, 1985; Bull *et al.*, 1991; Shen *et al.*, 1989). In the resting Mn(III) enzyme, the ligand geometry is distorted from trigonal bipyramidal toward octahedral in a way that should facilitate formation of an intermediate six-co-ordinate species during catalytic turnover. The existence of a cavity next to this co-ordination position provides driving force for the combination of substrate. Finally, reduction occurs without substantial rearrangement, as required if the activation energy for the overall reaction is to be kept small.

This research was supported by grants from the National Institutes of Health (GM16429) to M.L.L. and to Dr J. A. Fee (GM35189). Diffraction experiments were conducted at the Multiwire Area Detector Facility at the University of California, San Diego, and some of the computations were carried out at the San Diego Supercomputer Center. We are grateful to Dr J. A. Fee for his continuing interest in this work and to Drs Fee and Christopher Bull for discussions and comments. Dr Karl Törnroos, Stockholm University, made major contributions to the construction of the initial model of the structure, and Patricia Racenis assisted with the sequence alignments.

References

Bacquet, R. J., McCammon, A. J. & Allison, S. A. (1988). Ionic strength dependence of enzyme–substrate interactions. Monte-Carlo and Poisson–Boltzmann results for superoxide dismutase. *J. Phys. Chem.* **92** 7134–7141.

Barra, D., Schinina, M. E., Simmaco, M., Bannister, J. V., Bannister, W. H., Rotilio, G. & Bossa, F. (1984). The primary structure of human liver manganese superoxide dismutase. *J. Biol. Chem.* **259**, 12595–12601.

Barra, D., Schinina, M. E., Bannister, W. H., Bannister, J. V. & Bossa, F. (1987). The primary structure of iron-superoxide dismutase from *Photobacterium leiognathi*. *J. Biol. Chem.* **262**, 1001–1009.

Bashkin, J. S., Huffman, J. C. & Christou, G. (1986). Synthetic model approach to the manganese(III) acid phosphatase and its iron(III)-substituted form. *J. Amer. Chem. Soc.* **108**, 5038–5039.

Beck, Y., Bartfield, D., Yavin, Z., Levanon, A., Gorecki, M. & Hartman, J. R. (1988). Efficient production of active human manganese superoxide dismutase in *Escherichia coli*. *Biotechnology*, **6**, 930–935.

Benovic, J., Tillman, T., Cudd, A. & Fridovich, I. (1983). Electrostatic facilitation of the reaction catalyzed by manganese-containing and iron-containing superoxide dismutases. *Arch. Biochem. Biophys.* **221**, 329–332.

Bertini, I., Luchinat, C. & Monnanni, R. (1985). Evidence of the breaking of the copper imidazolate bridge in copper/cobalt substituted superoxide dismutase upon reduction of the copper(II) centers *J. Amer. Chem. Soc.* **107**, 2178–2179.

Bolin, J. T., Filman, D. J., Matthews, D. A., Hamlin, R. C. & Kraut, J. (1982). Crystal structures of *Escherichia coli* and *Lactobacillus casei* dihydrofolate reductase refined at 1·7 Å resolution. *J. Biol. Chem.* **257**, 13650–13662.

Borders, C. L., Jr, Horton, P. J. & Beyer, W. F., Jr (1989). Chemical modification of iron and manganese-containing superoxide dismutases from *Escherichia coli*. *Arch. Biochem. Biophys.* **268**, 74–80.

Bowie, J. U., Reidhaar-Olson, J. F., Lim, W. A. & Sauer, R. T. (1990). Deciphering the message in protein sequences: tolerance to amino acid substitutions. *Science*, **247**, 1306–1310.

Brock, C. J. & Walker, J. E. (1980). Superoxide dismutase from *Bacillus stearothermophilus*. Complete amino acid sequence of a manganese enzyme. *Biochemistry*, **19**, 2873–2882.

Brock, C. J., Harris, J. I. & Sato, S. (1976). Superoxide dismutase from *Bacillus stearothermophilus*. Preparation of stable apoprotein and reconstitution of fully active Mn enzyme. *J. Mol. Biol.* **107**, 175–178.

Bull, C. & Fee, J. A. (1985). Steady-state kinetic studies of superoxide dismutases: properties of the iron containing protein from *Escherichia coli*. *J. Amer. Chem. Soc.* **107**, 3295–3304.

Bull, C., Niederhoffer, E. C., Yoshida, T. & Fee, J. A. (1991). Kinetic studies of superoxide dismutases: properties of the manganese containing protein from *Thermus thermophilus*. *J. Amer. Chem. Soc.* in the press.

Burley, S. K. & Petsko, G. A. (1988). Weakly polar interactions in proteins. *Advan. Protein Chem.* **39**, 125–189.

Callahan, T. J., Gleason, W. B. & Lybrand, T. P. (1990). PAP: a protein analysis package. *Amer. Crystallogr. Ass. Abstr.* **18**, 73.

Cambillau, C. & Horjales, E. (1987). TOM: a FRODO superpackage for protein–ligand fitting with interactive energy minimization. *J. Mol. Graph.* **5**, 174–177.

Carlioz, A., Ludwig, M. L., Stallings, W. C., Fee, J. A., Steinman, H. M. & Touati, D. (1988). Iron superoxide dismutase: nucleotide sequence of the gene from *Escherichia coli* K12 and correlation with crystal structures. *J. Biol. Chem.* **263**, 1555–1562.

Chan, V. W. F., Bjerrum, M. J. & Borders, C. L., Jr (1990). Evidence that chemical modification of a positively charged residue at position 189 causes the loss of catalytic activity of iron-containing and manganese-containing superoxide dismutases. *Arch. Biochem. Biophys.* **279**, 195–201.

Clare, D. A., Blum, J. & Fridovich, I. (1984). A hybrid superoxide dismutase containing both functional iron and manganese. *J. Biol. Chem.* **259**, 5932–5936.

Day, V. W., Stults, B. R., Tasset, E. L. & Marianelli, R. S. (1975). Stereochemistry of 5 and 6-co-ordinate high-span manganese(III) porphyrins and their structural analogues. *Inorg. Nucl. Chem. Letters*, **11**, 505–509.

Ditlow, C., Johansen, J. T., Martin, B. M. & Svendsen, I. (1982). The complete amino acid sequence of manganese-superoxide dismutase from *Saccharomyces cerevisiae*. *Carlsberg Res. Commun.* **47**, 81–91.

Dougherty, H. W., Sadowski, S. J. & Baker, E. E. (1978). A new iron-containing superoxide dismutase from *Escherichia coli*. *J. Biol. Chem.* **253**, 5220–5223.

Fee, J. A. (1980). Superoxide, superoxide dismutases and oxygen toxicity. In *Metal Ion Activation of Dioxygen* (Spiro, T. G., ed.), pp. 209–237, Wiley & Sons, New York.

Fee, J. A., Shapiro, E. R. & Moss, T. H. (1976). Direct evidence for manganese(III) binding to the manganosuperoxide dismutase of *Escherichia coli* B. *J. Biol. Chem.* **251**, 6157–6159.

Fee, J. A., McClune, G. J., Lees, A. C., Zidovetski, R. & Pecht, I. (1981). The pH dependence of the spectral and anion binding properties of iron containing superoxide dismutase from *E. coli* B: an explanation for the azide inhibition of dismutase activity. *Israel J. Chem.* **21**, 54–58.

Fermi, G. (1975). Three-dimensional Fourier synthesis of human deoxyhaemoglobin at 2·5 Å resolution refinement of the atomic model. *J. Mol. Biol.* **97**, 237–256.

Fridovich, I. (1979). Superoxide and superoxide dismutases. In *Advances in Inorganic Biochemistry* (Eichhorn, G. L. & Marzelli, L. G., eds), vol. 1, pp. 67–90, Elsevier/North Holland, Amsterdam.

Hallewel, R. A., Mullenbach, G. T., Stempien, M. M. & Bell, G. I. (1986). Sequence of a cDNA coding for mouse manganese superoxide dismutase. *Nucl. Acids Res.* **14**, 9539

Hardman, K. D., Agarwal, R. C. & Freiser, M. J. (1982). Manganese and calcium binding sites of concanavalin A. *J. Mol. Biol.* **157**, 69–86.

Harris, J. I., Auffret, A. D., Northrop, F. D. & Walker, J. E. (1980). Structural comparisons of superoxide dismutases. *Eur. J. Biochem.* **106**, 297–303.

Heckl, K. (1988). Isolation of cDNAs encoding human manganese superoxide dismutase. *Nucl. Acids Res.* **16**, 6224.

Hendrickson, W. A. (1985). Stereochemically restrained refinement of macromolecular structures. *Methods Enzymol.* **115**, 252–270.

Hermans, J. & McQueen, J. E., Jr (1974). Computer manipulation of (macro)molecules with the method of local change. *Acta Crystallogr. sect. A*, **30**, 730–739.

Ho, Y.-S. & Crapo, J. D. (1987). Nucleotide sequences of cDNAs coding for rat manganese-containing superoxide dismutase. *Nucl. Acids Res.* **15**, 10070.

Ho, Y.-S. & Crapo, J. D. (1988). Isolation and characterization of complementary DNAs encoding human manganese-containing superoxide dismutase. *FEBS Letters*, **229**, 256–260.

Isobe, T., Fang, Y. I., Muno, D., Okuyama, T., Ohmori, D. & Yamakura, F. (1987). Amino acid sequence of iron-superoxide dismutase from *Pseudomonas ovalis*. *FEBS Letters*, **223**, 92–96.

Jones, T. A. (1982). FRODO, a graphics fitting program for macromolecules. In *Computational Crystallography* (Sayre, D., ed.), pp. 303–317, Clarendon Press, Oxford, U.K.

Jones, T. A. & Thirup, S. (1986). Using known substructures in protein model building and crystallography. *EMBO J.* **5**, 819–822.

Kabsch, W. & Sander, C. (1983). Dictionary of protein secondary structure: pattern recognition of hydrogen-bonded and geometrical features. *Biopolymers*, **22**, 2577–2637.

Karplus, P. A. & Schulz, G. (1987). Refined structure of glutathione reductase at 1·54 Å resolution. *J. Mol. Biol.* **195**, 701–729.

Kundrot, C. E. & Richards, F. M. (1987). Use of the occupancy factor in the refinement of solvent molecules in protein crystal structures. *Acta Crystallogr. sect. B*, **43**, 544–547.

Laudenbach, D. E., Trick, C. G. & Straus, N. A. (1989). Cloning and characterization of an *Anacystis nidulans* R2 superoxide dismutase gene. *Mol. Gen. Genet.* **216**, 455–461.

Lavelle, F., McAdam, M. E., Fielden, E. M. & Roberts, P. B. (1977). A pulse-radiolysis study of the catalytic mechanism of the iron-containing superoxide dismutase from *Photobacterium leiognathi*. *Biochem. J.* **161**, 3–11.

Leijonmarck, M. & Liljas, A. (1987). Structure of the C-terminal domain of the ribosomal protein L7/L12 from *Escherichia coli* at 1·7 Å. *J. Mol. Biol.* **195**, 555–580.

Lindqvist, Y. (1989). Refined structure of spinach glycolate oxidase at 2·0 Å resolution. *J. Mol. Biol.* **209**, 151–166.

Lipman, D. J. & Pearson, W. R. (1985). Rapid and sensitive protein similarity searches. *Science*, **227**, 1435–1441.

Lis, T., Matuszewski, J. & Jezowska-Trzebiatowska, B. (1977). Crystal structures of $K[Mn(H_2O)_2(mal)_2]$ and $K_3[Mn(mal)_3].2H_2O$. *Acta Crystallogr. sect. B*, **33**, 1943–1946.

Ludwig, M. L., Pattridge, K. A. & Stallings, W. C. (1986). Manganese superoxide dismutases. In *Manganese in Metabolism and Enzyme Function* (Schramm, V. L. & Wedler, F. C., eds), pp. 405–430, Academic Press, Orlando.

Marres, C. A. M., Van Loon, A. P. G. M., Oudshoorn, P., Van Steeg, H., Grivell, L. A. & Slater, E. C. (1985). Nucleotide sequence analysis of the nuclear gene coding for manganese superoxide dismutase of yeast mitochondria. *Eur. J. Biochem.* **147**, 153–161.

McAcam, M. E., Fox, R. A., Lavelle, F. & Fielden, E. M. (1977). A pulse-radiolysis study of the manganese-containing superoxide dismutase from *Bacillus stearothermophilus*. A kinetic model for the enzyme action. *Biochem. J.* **165**, 71–79.

Menendez-Arias, L. & Argos, P. (1989). Engineering protein thermal stability. *J. Mol. Biol.* **206**, 397–406.

Miller, S. (1989). The structure of interfaces between subunits of dimeric and tetrameric proteins. *Protein Eng.* **3**, 77–83.

Milner-White, E. J. (1987). Beta-bulges within loops as recurring features of protein structure. *Biochim. Biophys. Acta*, **911**, 261–265.

Milner-White, E. J. & Poet, R. (1986). Four classes of β-hairpins in proteins. *Biochem. J.* **240**, 289–292.

Parker, M. W. & Blake, C. F. (1988). Crystal structure of manganese superoxide dismutase from *Bacillus stearothermophilus* at 2·4 Å resolution. *J. Mol. Biol.* **199**, 649–661.

Pearson, W. R. (1990). Rapid and sensitive sequence comparison with FASTP and FASTA. *Methods Enzymol.* **183**, 63–98.

Phillips, F. L., Shreeve, F. M. & Skapski, A. C. (1976). Crystal and molecular structure of dichlorotris-(2-methylimidazole)manganese(II): a high-spin pentacoordinate complex of manganese. *Acta Crystallogr. sect. B*, **32**, 687–692.

Pick, M., Rabani, J., Yost, F. & Fridovich, I. (1974). The catalytic mechanism of the manganese-containing superoxide dismutase of *Escherichia coli* studied by pulse radiolysis. *J. Amer. Chem. Soc.* **96**, 7329–7333.

Ramachandran, G. N. & Sasisekharan, V. (1968). Conformation of polypeptides and proteins. In *Advances in Protein Chemistry* (Anfinsen, C. B., Jr, Anson, M. L., Edsall, J. T. & Richards, F. M., eds), vol. 23, pp. 283–438, Academic Press, New York.

Richards, F. M. (1985). Calculation of molecular volumes and areas for structures of known geometry. *Methods Enzymol.* **115**, 440–464.

Richards, F. M. & Kundrot, C. E. (1988). Identification of structural motifs from protein co-ordinate data: secondary structure and first-level supersecondary structure. *Proteins*, **3**, 71–84.

Richardson, J. S. (1981). The anatomy and taxonomy of proteins. *Advan. Protein Chem.* **34**, 167–339.

Richardson, J. S. & Richardson, D. C. (1989). In *Prediction of Protein Structure and Principles of Protein Conformation* (Fasman, G. D., ed.), pp. 1–98. Plenum Press, New York.

Ringe, D., Petsko, G. A., Yamakura, F., Suzuki, K. & Ohmori, D. (1983). Structure of iron superoxide dismutase from *Pseudomanas ovalis* at 2·8 Å resolution. *Proc. Nat. Acad. Sci., U.S.A.* **80**, 3879–3883.

Sato, S. & Harris, J. I. (1977). Superoxide dismutase from *Thermus aquaticus*. *Eur. J. Biochem.* **73**, 373–381.

Sato, S. & Nakazawa, K. (1978). Purification and properties of superoxide dismutase from *Thermus thermophilus* HB8. *J. Biochem.* **83**, 1165–1171.

Sato, S., Nakada, Y. & Nakazawa-Tomizawa, K. (1987). Amino-acid sequence of a tetrameric, manganese superoxide dismutase from *Thermus thermophilus* HB8. *Biochim. Biophys. Acta*, **912**, 178–184.

Schinina, M. E., Maffey, L., Barra, D., Bossa, F., Puget, K. & Michelson, A. M. (1987). The primary structure of iron superoxide dismutase from *Escherichia coli*. *FEBS Letters*, **221**, 87–90.

Shen, J., Subramaniam, S., Wong, C. F. & McCammon, J. A. (1989). Superoxide dismutase: fluctuations of the structure and solvation of the active site channel studied by molecular dynamics simulation. *Biopolymers*, **28**, 2085–2096.

Sibanda, B. L. & Thornton, J. M. (1985). β-Hairpin families in globular proteins. *Nature (London)*, **316**, 170–174.

Sines, J., Allison, S., Wierzbicki, A. & McCammon, J. A. (1990). Brownian dynamics simulation of the superoxide-superoxide dismutase reaction: iron and manganese enzymes. *J. Phys. Chem.* **94**, 959–961.

Stallings, W. C., Powers, T. B., Pattridge, K. A., Fee, J. A. & Ludwig, M. L. (1983). Iron superoxide dismutase from *Escherichia coli* at 3·1 Å resolution: a structure unlike that of copper/zinc protein at both monomer and dimer levels. *Proc. Nat. Acad. Sci., U.S.A.* **80**, 3884–3888.

Stallings, W. C., Pattridge, K. A., Strong, R. K. & Ludwig, M. L. (1984). Manganese and iron superoxide dismutases are structural homologs. *J. Biol. Chem.* **259**, 10695–10699.

Stallings, W. C., Pattridge, K. A., Strong, R. K. & Ludwig, M. L. (1985). The structure of manganese superoxide dismutase from *Thermus thermophilus* at 2·4 Å resolution. *J. Biol. Chem.* **260**, 16424–16432.

Stallings, W. C., Metzger, A. L., Pattridge, K. A., Fee, J. A. & Ludwig, M. L. (1991). Structure–function relationships in Fe and Mn-superoxide dismutases. *Free Rad. Res. Comm.* in the press.

Steinman, H. M. (1978). The amino acid sequence of mangano superoxide dismutase from *Escherichia coli* B. *J. Biol. Chem.* **253**, 8708–8720.

Stenkamp, R. E., Sieker, L. C. & Jensen, L. H. (1983). Adjustment of restraints in the refinement of methemerythrin and azidomethemerythrin at 2·0 Å resolution. *Acta Crystallogr. sect. B*, **39**, 697–703.

Stoddard, B. L., Howell, P. L., Ringe, D. & Petsko, G. A. (1990). The 2·1 Å structure of iron superoxide dismutase from *Pseudomonas ovalis*. *Biochemistry*, **29**, 8885–8893.

Takao, M., Kobayashi, T., Oikawa, A. & Yasui, A. (1989). Tandem arrangement of photolyase and superoxide dismutase genes in *Halobacterium halobium*. *J. Bacteriol.* **171**, 6323–6329.

Takeda, Y. & Avila, H. (1986). Structure and gene expression of the *E. coli* Mn-superoxide dismutase gene. *Nucl. Acids Res.* **14**, 4577–4589.

Texter, F. L., Radford, S. E., Laue, E. D., Perham, R. N., Miles, J. S. & Guest, J. R. (1988). Site-directed mutagenesis and ^{1}H NMR spectroscopy of an interdomain segment in the pyruvate dehydrogenase multienzyme complex of *Escherichia coli*. *Biochemistry*, **27**, 289–296.

Thangaraj, H. S., Lamb, F. I., Davis, E. O. & Colston, M. J. (1989). Nucleotide and deduced amino acid sequence of *Mycobacterium leprae* manganese superoxide. *Nucl. Acids Res.* **17**, 8378.

Vincent, J. B. & Christou, G. (1989). Higher oxidation state manganese biomolecules. *Adran. Inorg. Chem.* **33**, 197–257.

Wagner, U., Werber, M. M., Beck, Y., Hartman, J. R., Frolow, F. & Sussman, J. (1989). Characterization of crystals of genetically engineered human manganese superoxide dismutase. *J. Mol. Biol.* **206**, 787–788.

Watenpaugh, K. A., Sieker, L. & Jensen, L. H. (1980). Crystallographic refinement of rubredoxin at 1·2 Å resolution. *J. Mol. Biol.* **138**, 615–633.

Weighardt, K. (1989). The active sites in manganese-containing metalloproteins and inorganic model complexes. *Angew. Chem. Int. Ed.* **28**, 1153–1172.

Weisiger, R. A. & Fridovich, I. (1973). Mitochondrial superoxide dismutases: site of synthesis and intramitochondrial localization. *J. Biol. Chem.* **248**, 4793–4796.

White, J. A. & Scandalios, J. G. (1986). Isolation and characterization of a cDNA for mitochondrial manganese superoxide dismutase (SOD-3) of maize and its relation to other manganese superoxide dismutases. *Biochim. Biophys. Acta*, **951**, 61–70.

Yaffa, B., Rachel, O., Boaz, A., Levanon, A., Marian, G. & Hartman, J. R. (1987). Human Mn superoxide dismutase cDNA sequence. *Nucl. Acids Res.* **15**, 9076.

Edited by R. Huber